U.PORTO
FEUP FACULDADE DE ENGENHARIA
UNIVERSIDADE DO PORTO

University of Porto

Faculty of Engineering

Hydrodynamic analysis of bio-inspired shapes for Autonomous Underwater Vehicle

Henrique Miguel Martinho Moreira Carneiro

Supervisors:
Prof. Dr. Alexandre Afonso (FEUP)
Dr. Adriano Lima (INEGI)

Dissertation submited to the University of Porto
in partial satisfaction of the requirements for the
degree of Master in Mechanical Engineering.

July 2019

Contact information:
Henrique Carneiro
Institutional email: up201403195@fe.up.pt

This document was typeset with LaTeX using the **CVR** thesis template.

Abstract

Autonomous underwater vehicles have been gathering increased interest as sustainability and automation are increasingly important topics in underwater activities. Simultaneously, bio-inspired solutions have proven to be remarkably efficient and a great advantage over traditional approaches. Several studies have been performed on fish-like swimming performance, most of which mathematically describing the motion observed in experimental studies of live animals. This work composes a numerical study on the performance of *anguilliform* motion at several conditions relevant for bio-inspired underwater vehicles.

A numerical model was first tested with standard torpedo-shaped hulls at various velocities and angles of attack. Effects of mesh refinement were studied and drag and lift force were compared to literature studies for validation purposes.

This model was then applied to periodic *anguilliform* swimming motion, studying the thrust and drag forces for several tail-beat frequencies (Strouhal number) at four different Reynolds numbers ($Re = 500, 2000, 4000, 8000$). The critical Strouhal number was found for each Re value and the Froude efficiency was calculated for every critical Strouhal number.

Resumo

Os veículos submarinos autónomos têm ganho um interesse acrescido já que a sustentabilidade e a automação são assuntos cada vez mais importantes em operações subaquáticas. Simultaneamente, soluções bio-inspiradas provaram ser extremamente eficientes e uma grande vantagem em relação a abordagens mais tradicionais. Foram realizados vários estudos acerca do desempenho de espécies marinhas, maioritariamente na descrição matemática dos movimentos observados de espécies vivas em testes experimentais. Este trabalho constitui um estudo numérico do desempenho de formas anguiliforme em várias condições relevantes para os veículos bio-inspirados.

Um modelo numérico foi inicialmente testado em formas padrão de submarinos a várias velocidades e ângulos de ataque. Os efeitos do refinamento da malha foram estudados, e as forças de arrasto e sustentação foram comparadas com valores da literatura, como forma de validação.

Este modelo foi então aplicado para o estudo de movimentos anguiliforme periódicos, analisando as forças de impulsão e arrasto para várias frequências de oscilação (número de Strouhal) a quatro números de Reynolds diferentes ($Re = 500, 2000, 4000, 8000$). Com base nos dados, foi identificado o número de Strouhal crítico para cada valor de Re e para cada número de Strouhal critico foi calculada a eficiência de Froude.

Contents

List of Figures

List of Tables

Chapter 1

Introduction

1.1 Thesis context

The biodiversity and value of marine resources have driven the exploration of aquatic environments for benefits in numerous areas, from aquaculture to deep ocean mapping and prospecting. The rising importance of these activities demand for higher sustainability and efficiency.

Particularly in aquaculture, this sustainability involves monitoring of habitat to address common problems as pollution and diseases and collect data for fish growth. These activities are mostly performed by human divers that besides disturbing the creatures, their actions are restricted in low-visibility conditions [1].

Deep ocean activities, such as prospecting and periodic inspections of structures for oil and gas industries, and geoscience applications as floor mapping and geothermal studies, make human diving impractical and the use of Remotely Operated Vehicles (ROVs) expensive and time-consuming [2].

As such, there is an increased interest in Autonomous Underwater Vehicles (AUVs) by many industries to carry out monitoring, surveillance and exploration missions. These vehicles usually have torpedo shapes and utilize propellers to thrust and maneuver, which make them lack secrecy and maneuverability, affecting the missions effectiveness.

To address this problem, AUV concepts have been designed with shapes resembling marine species in an effort to benefit from their superior capabilities of stability, maneuverability, velocity, efficiency and silent movement. Vehicles of various shapes enabled the use of AUVs in a wide variety of environments, however each one of them is limited to the type of environment it was designed for. AUVs designed to operate in large areas requiring high energy efficiency and speed are not capable of engaging in missions in confined spaces. Similarly, AUVs designed for high maneuverability underperform in large distance and duration missions due to their high drag coefficient [3].

Therefore, there is a high demand for AUVs capable of changing between a few selected shapes, each one designed to excel in a specific type of environment, taking advantage of their hydrodynamic features to increase performance and efficiency. As missions involving present day bio-inspired AUVs are limited by this vehicles endurance, usually ranging from 1 to 10 hours [4–6], the use of shape adapting techniques would certainly revolutionize marine operations given their capability of self-sustainability, by using its reshaping ability to harness energy from ocean currents or waves by emerging to the surface. By using multiple vehicles alternating operation and charging processes between them, it is possible to perform operations indefinitely.

TECMAR is the Sea Technologies group at INEGI, Institute of Science and Innovation in Mechanical and Industrial Engineering, which promotes and develops solutions adjusted to industrial needs particularly related to the maritime industry. With this project, TECMAR aims to advance on the knowledge required to design and build a fully functioning bio-inspired AUV.

1.2 Objectives

Conceptual biomimetic AUVs are being designed and built all over the world because of their obvious advantages over traditional torpedo AUVs. TECMAR understands the potential of these vehicles and is pursuing the building of a biomimetic AUV capable of altering shapes to provide a self-sustainable autonomous operating vehicle. The focus of this work is to get some initial insight on what shapes are best suited for the diverse operating modes and how to optimize those shapes, collecting relevant data of hydrodynamic variables that characterize their performance. To perform computational fluid dynamics (CFD) simulations, the software ANSYS Fluent will be used, limited to academic license.

This thesis studies numerically traditional torpedo-shaped AUVs to validate the numerical model. Afterwards, we will study numerically an *anguilliform* swimming motion to understand the effect of different conditions in its locomotive performance.

1.3 Outline

This thesis is structured in 6 chapters and 1 appendix.

Chapter 2 gives a literature review of concepts and definitions of fluid mechanics as well as the state of the art of current AUV and bio-inspired AUV solutions.

Chapter 3 presents the governing equations of the fluid flow and the assumptions made. It then exposes the numerical modelling used to solve those equations.

Chapter 4 provides a validation for the numerical model adopted using bare hull AUVs in order to deem the results credible.

Chapter 5 presents and discusses the results for *anguilliform* swimming motion simulations based on literature theory.

Chapter 6 covers the conclusions achieved and gives insight of possible future work to be performed.

Apendix A presents the User-Defined Function (UDF) used to define the mesh motion in ANSYS Fluent.

Chapter 2

Literature review

2.1 Bare hull hydrodynamics

Energy efficiency is one of the most important characteristics of any vehicle and therefore any submarine is designed to achieve a certain speed with the least power necessary. It is then essential to reduce the resistance or drag of the hull which can be due to friction or form.

Friction or viscous resistance is caused by the shear stresses as water flows over the hull surface and is dependent on the viscosity of the water, the wetted surface (the surface in contact with the fluid) and the surface roughness [7]. It represents about 60% to 70% of the total resistance for submarines [8].

Form or pressure resistance is caused by the shape of the hull which induces a local velocity flow field that has zones with higher velocity and zones with lower velocity than the hull speed. It can be minimized by having a streamline-shaped body and increasing the L/D ratio [8], where L is the hull length and D the maximum diameter. However, increasing the L/D ratio increases the wetted surface area and thus the skin friction drag, requiring a compromise. Joubert [9] states that an L/D ratio ratio of 6 to 7 minimizes the total resistance.

Research has shown that the ideal shape to reduce resistance is one with an ellipsoidal nose, a paraboloidal tail and with no constant diameter zone [9]. Figure 2.1 is an example of this ideal shape.

Figure 2.1: Example of an ideal shape according to Joubert [9]. Adapted from [10].

Several studies on hydrodynamic behavior of axisymmetric bodies have developed optimized hull shapes, namely Huang [11] afterbodies, in which the author provides offset points for two optimized geometries and Myring [12] equations that specify the shape of nose and tail regions of the hull.

2.2 Fish swimming mechanics

Fish have developed a great variety of swimming propulsors called fins to allow them to move effectively in the water. Figure 2.2 exhibits the terminology used to identify the fins and other morphological features.

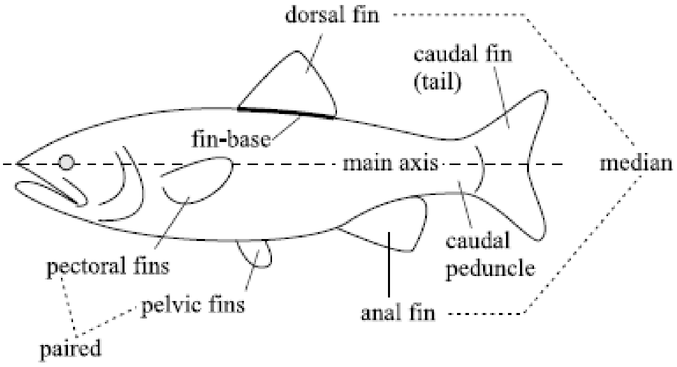

Figure 2.2: Terminology of morphological features of fish [13]

Fish locomotion, as first presented by Breder [14], can be classified into 12 modes according to the propulsive contributions of body and fins and the extent to which propulsion lies along the gradient of oscillatory and undulatory motion [15]. Based on the major actuation portion of the body, these modes can be grouped into two major propulsion modes: the Body-Caudal Fin (BCF) propulsion and the Median-Paired Fin (MPF) propulsion. BCF propulsion is generated by large body displacement, producing greater thrust, velocity and cruising efficiency whereas MPF propulsion is generated by coordinated movements of small control fins allowing for high propulsive efficiencies at low velocities and precise control of position and stabilization [16]. More than 85% of fish swim by undulating BCF [17]. The 12 modes of fish locomotion are presented in figure 2.3.

Particularly, *anguilliform* and *thunniform* modes are of great interest for AUVs as each one has very distinct and unique features, capable of excelling in opposite conditions.

Anguilliform swimmers such as eels and lampreys are characterized by their long, slender and flexible body where its undulation is responsible for producing thrust at the expense of drag. The greatest advantage of this swimming mode is its dexterous maneuverability allowing them to swim in tight spaces [15, 16, 18].

Thunniform swimmers such as tunas and some sharks have streamlined body shapes, very narrow peduncles and high aspect ratio crescent shaped caudal fins. They are the fastest swimmers and extremely efficient at high velocities while sacrificing efficiency and maneuverability at low velocities [15, 16, 18].

A bio-inspired AUV capable of switching between these two swimming modes is of great utility as it is able to swim effectively and efficiently in almost any aquatic environment.

In this work, only *Anguilliform* swimming motion will be studied.

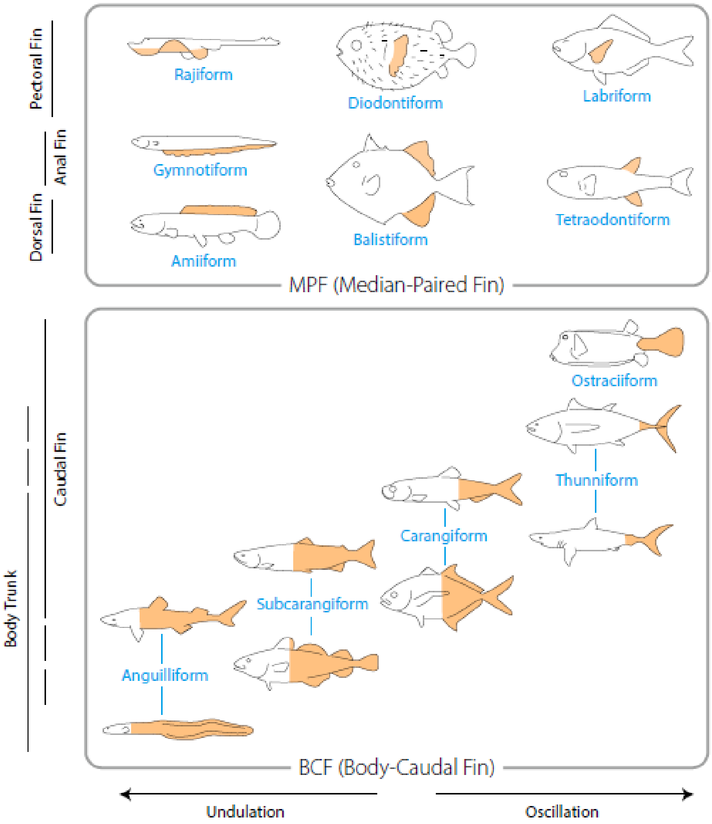

Figure 2.3: Swimming modes sorted by the types of primary movements on the vertical axis and the breadth of the primary movement regions on the the horizontal axis [13].

2.2.1 Swimming parameters

The following four non-dimensional parameters are used to characterize the swimming movement. Figure 2.4 shows the dimensions used.

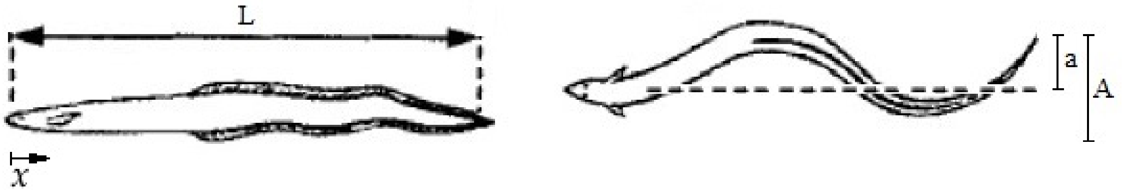

Figure 2.4: Relevant dimensions for an *anguilliform* body. Adapted from [19].

Reynolds number (*Re*) is defined as the ratio of inertial forces to viscous forces and is used here as a non-dimensional velocity. It is given by

$$Re = \frac{U \cdot L}{\nu} \tag{2.1}$$

where U is the swimming velocity, L is the length of the main thrust propulsor, the body in *anguilliform* mode and ν is the kinematic viscosity of water. Often in literature, the body length distance traveled per second (BL/s) is used instead as a velocity parameter, despite being dimensional.

Strouhal number (St) is used to describe oscillating flow mechanisms and in this work it represents a frequency parameter. It is defined as

$$St = \frac{fA}{U} \tag{2.2}$$

where f is the tail beat frequency and A is the maximum lateral excursion of the tail (peak-to-peak amplitude).

Non-dimensional wavelength (λ/L) represents the wavelength of the traveling wave per body length.

These λ/L values taken from experimental studies are often dissimilar. Vorus and Taravella [20] experiment with live lamprey recorded a non-dimensional wavelength of 0.8 whereas Hultmark et al [21] experiment with the same species registered 0.642. Tytell and Lauder [22] recorded a mean value of 0.604 for American eels while Wardle et al. [23] documented a non-dimensional wavelength value of 0.59 for eels and lampreys.

Sometimes, the slip velocity U/V, where V is the traveling wave speed, is used instead of non-dimensional wavelength. Both approaches are correct, however the slip velocity changes with the tail-beat frequency. For the scope of this study it is best to use the non-dimensional wavelength [24].

Non-dimensional amplitude (a/L) represents the maximum value of the amplitude envelope (at the tail) per body length, such that $a = A/2$.

Similarly to wavelength, the recorded values differ between species and experiments. Hultmark et al. [21] registered a value of 0.089 for their lamprey experiment, Tytell and Lauder [22] documented 0.069 for American eels and Vorus and Taravella [20] states 0.1 as the maximum value of the amplitude envelope of juvenile lampreys.

2.2.2 *Anguilliform* motion equation

In 2011, Vorus and Taravella [20] presented a theory for the hypothesis that steady *anguilliform* swimming motion is purely reactive, meaning that no vortex wake is left downstream. Contrary to *carangiform* and *thunniform* modes where vortex streams are shed from tail, fins and body to achieve partial vortex cancellation, it is argued that in *anguilliform* mode, to maximize efficiency, vortex shedding does not occur at all. Since the vortex wake is absent, the wake-induced drag is null, implying high propulsive efficiency. Under these conditions, the thrust produced is second order in displacement amplitude, meaning that for a given amplitude, the high efficiency is only achieved at relatively low speeds [20].

Contrary to most of the research done in *anguilliform* swimming behavior at high Reynolds number that implies ideal flow theory with vortex shedding and skin friction corrections to account for viscosity, the theory from Vorus and Taravella [20] proposes that no lifting forces nor circulation are generated through the body and the thrust is produced by body accelerations through hydrodynamic added mass [20].

The motion is given by the displacement, h, along the length of the eel on the horizontal direction, x, for any given time, t, in equation (2.3).

$$h(x,t) = \frac{a}{L}\left[\sin\left(\frac{2\pi}{L}\left(\frac{V}{U}x - Vt\right)\right) - \sin\left(\frac{2\pi}{L}(x - Vt)\right)\right] \tag{2.3}$$

The traveling wave velocity, V, is given by

$$V = fL \tag{2.4}$$

and as stated in section 2.2.1, the slip velocity U/V can be replaced by the non-dimensional wave length λ/L.

Equation (2.3) then becomes

$$h(x,t) = a\left[\sin\left(2\pi\left(\frac{1}{\lambda/L}\frac{x}{L} - ft\right)\right) - \sin\left(2\pi\left(\frac{x}{L} - ft\right)\right)\right] \tag{2.5}$$

This movement equation differs from others in literature. Borazjani and Sotiropoulos [24], Hultmark et al. [21] and Tytell and Lauder [22] state that the equation describing the lateral undulations of *anguilliform* fish body is given by

$$h(x,t) = a(x)\sin(kx - \omega t) \tag{2.6}$$

where k is the wave number of the body undulations that corresponds to a wavelength, λ, and ω is the angular frequency.

These approaches differ only slightly on the amplitude envelope, $a(x)$, given by

$$a(x) = \frac{a}{L}e^{\alpha(x-1)} \tag{2.7}$$

where α is the amplitude growth rate taking the value of 1 in Borazjani and Sotiropoulos [24], 2.18 in Hultmark et al. [21] and 2.76 in Tytell and Lauder [22].

Despite the apparent amplitude envelope and non-dimensional amplitude values differences between these three approaches and the one in Vorus and Taravella [20], Figure 2.5, showing the body centerline at time $t = 0$ for all four approaches, indicates they are all quite similar, as would be expected given the similarities between the studied species.

2.2.3 Force decomposition and efficiency

Borazjani and Sotiropoulos [25] proposed a decomposition of the axial force (x-direction) $F(t)$ in thrust $T(t)$ and drag $D(t)$ as follows:

$$T(t) = T_\mathrm{p} + T_\mathrm{v} = \frac{1}{2}\left(\int_A -pn_3\mathrm{d}A + \left|\int_A pn_3\mathrm{d}A\right|\right) + \frac{1}{2}\left(\int_A \tau_{3j}n_j\mathrm{d}A + \left|\int_A \tau_{3j}n_j\mathrm{d}A\right|\right) \tag{2.8}$$

$$D(t) = (D_\mathrm{p} + D_\mathrm{v}) = \frac{1}{2}\left(\int_A -pn_3\mathrm{d}A - \left|\int_A pn_3\mathrm{d}A\right|\right) + \frac{1}{2}\left(\int_A \tau_{3j}n_j\mathrm{d}A - \left|\int_A \tau_{3j}n_j\mathrm{d}A\right|\right) \tag{2.9}$$

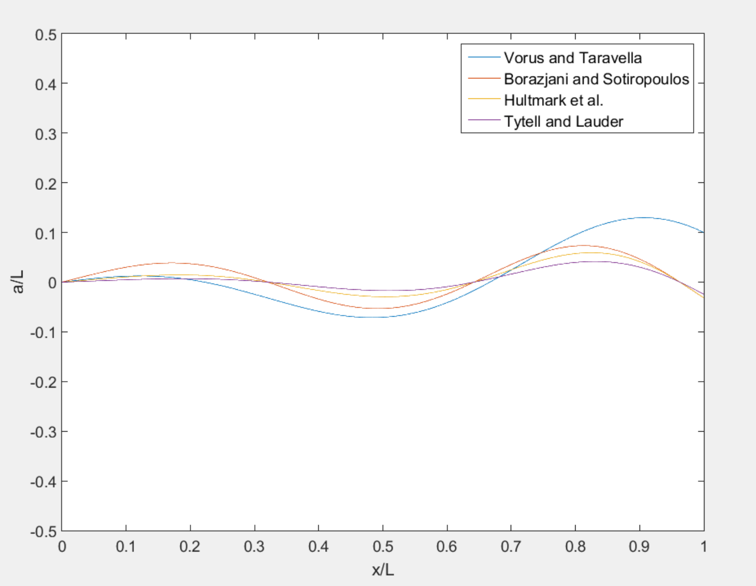

Figure 2.5: Comparison of centerline positions for motion equations given by Vorus and Taravella [20], Borazjani and Sotiropoulos [24], Hultmark et al. [21] and Tytell and Lauder [22].

where n_j is the j^{th} component of the unit normal vector on dA and τ_{ij} is the viscous stress tensor. The indices i and j represent the axis directions, 3 being the x direction. The subscripts p and v represent the pressure and viscous contributions, respectively.

The total force is then

$$F(t) = T(t) + D(t) \tag{2.10}$$

and is nondimensionalized as

$$C_F = \frac{F(t)}{\rho U^2 L^2} \tag{2.11}$$

where ρ is the density of the fluid.

The power loss due to lateral undulations of the body is given by:

$$P_{\text{side}} = \int -pn_2\dot{h}\mathrm{d}A + \int \tau_{2j}n_j\dot{h}\mathrm{d}A \tag{2.12}$$

where $\dot{h}$ is the time derivative of the lateral displacement (index 2 direction), i.e. the velocity of the lateral undulations.

According to Tytell and Lauder [22], the Froude propulsive efficiency, η, for constant inline speed is written as:

$$\eta = \frac{\text{Useful power}}{\text{Total power}} = \frac{\overline{T}U}{\overline{T}U + \overline{P_{\text{side}}}} \tag{2.13}$$

where $\overline{(\cdot)}$ denotes the average value over a swimming cycle.

According to elongated body theory (EBT) by Lighthill [26], the Froude efficiency for steady swimming is given by:

$$\eta_{\text{EBT}} = \frac{1}{2}(1 + \beta) \tag{2.14}$$

where $\beta = U/V$, as defined above, is the slip velocity.

Later, Cheng and Blickhan [27] proposed an improvement on the EBT efficiency formula, equation (2.15), taking into account the slope of the fish tail.

$$\eta_{\mathrm{EBT}-2} = \frac{1}{2}(1+\beta) - \frac{1}{2}\alpha^2 \frac{\beta^2}{1+\beta} \tag{2.15}$$

with α being defined as:

$$\alpha = \frac{\lambda}{2\pi} \frac{\dot{h}(L)}{h(L)} \tag{2.16}$$

where $h(L)$ is the undulation amplitude and $\dot{h}(L)$ is its derivative relative to x, at the tail.

Note that equation (2.12) is only valid for steady inline swimming, when the thrust force is perfectly balanced by the drag force, i.e. the average of $F(t)$ over a swimming cycle is zero. As this condition occurs only at a specific Strouhal number, denoted critical Strouhal number, St_{crit}, the propulsive efficiency given by equation (2.12) can only be computed at that St value [25].

2.3 State-of-the-art underwater vehicles

Underwater vehicles without a human occupant are known as Unmanned Underwater Vehicles (UUVs) and are classified into Remotely Operated Underwater Vehicles (ROV) if controlled remotely by a human operator and Autonomous Underwater Vehicles (AUVs) if controlled by an on-board computer.

Conventional AUVs typically range in length from 1.5 to 5.5 meters and in weight from 20 to 1400 kilograms [28]. While capable of velocities from 0.5 to 5 meters per second, vehicles usually move at 1 to 2 meters per second [28–30]. They generally have torpedo shaped hulls for minimum drag and are slightly positively buoyant to ensure the vehicle surfaces if control systems fail.

AUVs can be propeller-driven or buoyancy-driven. Buoyancy driven vehicles are often called gliders as they control buoyancy by moving internal ballast and using the descent and ascent movements to glide forward through hydrofoils, having an undulating trajectory. While not achieving the same cruising velocities as propeller-driven vehicles, gliders have significantly greater endurance, lasting for months or thousands of kilometers before recharging [31]. Propeller-driven AUVs, despite higher velocities, are very inefficient at low speeds and maneuvering and in aquaculture applications they can even cause low yield as they produce loud noise and vibrations that disturb fish [1]. However, their ability to maintain a linear trajectory through the water makes them well suited for geoscience applications requiring constant altitude such as seafloor mapping [29]. Figure 2.6 presents some examples of conventional AUVs.

Bio-inspired AUVs are autonomous underwater vehicles that are shaped and swim as a specific type of fish to benefit from its superior capabilities. These capabilities are mainly high efficiency, high velocity, silent swimming and good maneuverability and stability, and different marine species feature different capabilities.

Robotic fishes started to appear in the 1970s decade based on BCF propulsion species. In 1994, the Massachusetts Institute of Technology (MIT) designed and built the first

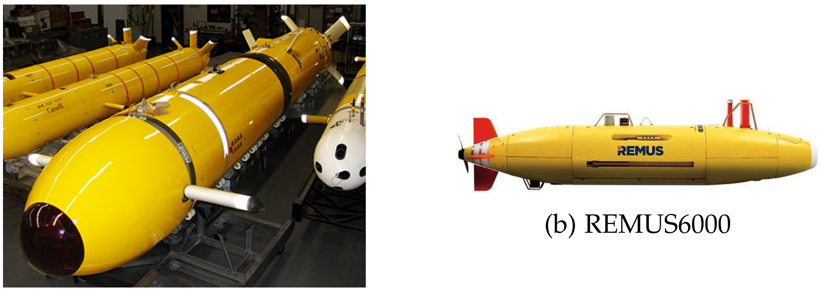

(a) Theseus

(b) REMUS6000

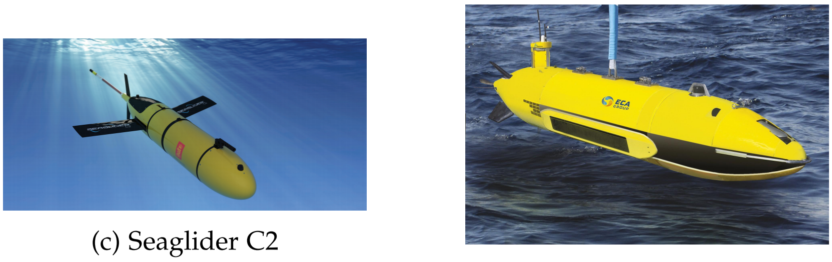

(c) Seaglider C2

(d) A-27M

Figure 2.6: Some examples of conventional AUVs. (a) Theseus was designed to lay fiber optic cable on the seafloor [32]. (b) REMUS6000 is part of the REMUS AUVs series and is capable of reaching 6000 meters of depth [33]. (c) Seaglider C2 is a commercial shallow water glider capable of large buoyancy alterations [34]. (d) A-27M is a military AUV capable of carrying out mine, shipwreck and aircraft detection at the seafloor [35].

robotic fish of the RoboTuna project and discovered that it was more maneuverable and energy efficient than conventional AUVs [36]. The robot mimicked a tuna for its high cruising velocities. Later, they build the RoboPike, inspired on a pike for its explosive accelerations [37]. In 2007, Low et al. [38] designed a robotic eel using *anguilliform* mode and Suzumori et al. [39] developed a manta ray robot. Figure 2.7 shows these robotic fishes.

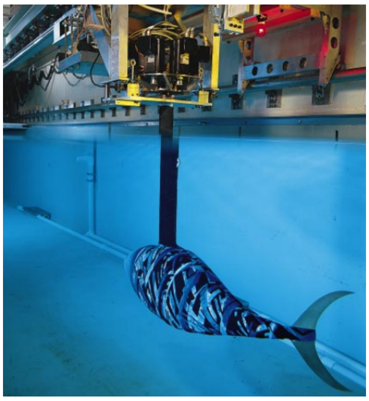

(a) RoboTuna

(b) RoboPike

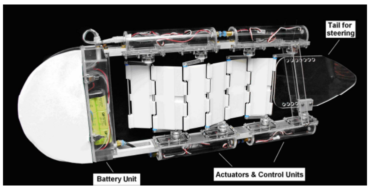

(c) Robotic eel

(d) Robotic manta ray

Figure 2.7: Some examples of robotic fish. (a) RoboTuna created by MIT, Triantafyllou et al. [36]. (b) RoboPike created by MIT, Kumph et al. [37]. (c) Prototype of a robotic eel designed and built by Low et al. [38]. (d) Robotic manta ray developed by Suzumori et al. [39].

Chapter 3

Governing equations and numerical methods

In this chapter, the governing equations of fluid dynamics are presented and a description of the numerical methods used in this work are given.

3.1 Motivation for numerical modeling

Numerical methods are used to achieve approximate results of problems whose equations cannot be solved analytically or when experimental methods are impractical [40]. The simulation tools used to solve these equations can be from commercial codes that from the users point of view operate as a black box, in the sense that it is possible to get results by giving input without knowing what is happening inside. This ignorance of what happens inside the simulation tool can lead to wrong or meaningless solutions [41].

The numerical tool solves a set of mathematical equations that model a physical problem based on physical principles and assumptions (i.e., conservation and incompressibility) and which are dictated by the user inputs. The tool obtains a numerical solution calculating specific variables at specific points of the domain, which are carried over to post-processing [41].

3.2 Governing equations

The governing equations of fluid dynamics are based on the laws of mechanics: the conservation of mass and the conservation of momentum. If the flow is compressible, the first law of thermodynamics is also taken into account and the conservation of energy is considered [42]. In this study, the fluid will be considered incompressible and the flow isothermic.

The governing equations can be written in differential form or integral form. In the differential form, the laws of mechanics are applied to an infinitesimal fluid particle and in the integral form they are applied to a finite volume in flow domain.

The differential form of mass conservation represented by equation (3.1) defines that the mass of an infinitesimal fluid particle moving within the flow cannot change. As fluid is incompressible, it implies that the volume of an infinitesimal fluid particle also cannot change, and the mass conservation becomes:

$$\frac{\partial \rho}{\partial t} + \nabla \cdot (\rho \vec{u}) = 0 \tag{3.1}$$

where $\vec{u}$ is the velocity vector, ρ the fluid density, $\nabla \cdot ()$ the divergence operator.

The conservation of momentum is the Newton second law applied to an infinitesimal fluid particle, meaning that for the differential form of momentum conservation - equation (3.2), the sum of the forces acting on the particle, namely the pressure force and the viscous force, are equal to the rate of change of its momentum:

$$\rho \frac{\partial \vec{u}}{\partial t} + \nabla \cdot (\rho \vec{u} \vec{u}) = -\nabla p + \nabla (\mu \nabla \cdot \vec{u}) \tag{3.2}$$

where μ is the fluid dynamic viscosity and $\nabla ()$ is the gradient operator.

The integral form of mass conservation - equation (3.3) defines that the mass going out of the control volume is equal to the mass coming into it, meaning that the net mass flow rate through the surface is zero. Considering incompressible flow, it can be said that the net volumetric flow rate through the control volume surface S is zero.

The integral form of momentum conservation - equation (3.4) sets out that the net momentum flow rate is equal to the net viscous and pressure forces acting on the control volume V.

$$\int_S \rho \left(\vec{u} \cdot \hat{n} \right) \mathrm{d}S = 0 \tag{3.3}$$

$$\int_V \rho \frac{\partial \vec{u}}{\partial t} \mathrm{d}V + \int_S \rho(\vec{u}\vec{u}) \cdot \hat{n} \ \mathrm{d}S = \int_S -p\hat{n} \ \mathrm{d}S + \vec{F}_{visc} \tag{3.4}$$

where $\hat{n}$ is the surface unit normal vector and $\vec{F}_{visc}$ is the viscous force.

These equations are solved for each control volume defined by the mesh, whose size affects the precision of the results. Reducing the control volumes size provides more precise results, yet increasing the calculation time as it demands more computational power. However as these equations are partial differential equations, coupled and non-linear, analytical solutions are very limited. In this work, ANSYS Fluent will be used to solve them approximately.

3.3 Numerical method: Finite Volume Method

The numerical technique that will be used to solve these partial differential equations is the Finite Volume Method (FVM). It is used by ANSYS Fluent as well as by several other CFD software packages [43–45]. The basic principle of FVM is to divide the flow domain into numerous small control volumes and apply the integral form of the conservation equations to each of them. As those continuous equations can not be solved analytically they are converted to a set of discrete algebraic equations for each control volume [46]. In the case of ANSYS Fluent the quantities are calculated at volume centers and are averaged and interpolated to get the values at the control volume surfaces, which introduces an error called discretization error [47]. This error can be reduced by using more control volumes in the domain. The discrete algebraic equations are still non-linear so they need to be linearized about a guess value in order to be solved iteratively, updating the guess value in each iteration [41]. This linearization introduces another error called linearization error that can be reduced by increasing the number of iterations.

The main advantage of FVM is that the conservation is directly applied to each finite volume. Since the method evaluates the fluxes at the surfaces, the flux leaving one volume is the same as the flux entering the adjacent one [48]. An additional advantage is its flexibility that allows it to be used with structured and unstructured meshes, being especially useful to simulate flow around complex geometries [49].

3.4 Software description

3.4.1 Pre-processing

3.4.1.1 Mesh generation

The first aspect of pre-processing is the geometry definition. Simple geometries can be defined through points or equations while complex geometries are usually defined in STL (STereoLithography) file format which consists of 3D surface tessellated into a series of unstructured triangles [50]. In ANSYS Workbench, the geometry can either be imported from a file or drawn using ANSYS Design Modeler or ANSYS SpaceClaim.

The most important part of pre-processing is the mesh generation. It consists in the subdivision of the domain into smaller non-overlapping subdomains (elements or cells) where the governing equations are solved numerically determining the discrete values of pressure, velocity and other variables of interest [51]. The accuracy of the CFD solution is not only influenced by the size, and thus, the number of cells in the mesh, as stated above, but also by the type of mesh, the order of accuracy of the numerical method, and the adequacy of the numerical methods chosen to describe the physics of the problem [51]. This accuracy comes with the cost of additional computational power and computational time requirements.

The cells can be of several shapes. 2D meshes usually use triangle or quadrilateral cells while elements of 3D meshes are generally tetrahedral or hexahedral. The mesh can be classified into structured or unstructured based on the cells connectivity. In a structured mesh each cell has the same number of neighboring cells, they follow an uniform pattern and are usually quadrilaterals (2D) or hexahedron (3D), while in an unstructured mesh there is not a regular pattern and its cells are usually triangles (2D) or tetrahedrons (3D). Figure 3.1 illustrates the aspect of these two types of mesh.

The advantage of structured meshes lies in its connectivity which makes it faster to solve, while unstructured meshes are better suited for complex geometries as the skewness is not as intense as in structured grids that can lead to unphysical solutions [52]. As the geometries used in this study are fairly complex, a mostly tetrahedral mesh was used.

3.4.1.2 Boundary conditions

In order to solve the system of equations it is necessary to define the boundary conditions. In ANSYS Fluent there are several types of of boundary conditions and the ones used in this study were:

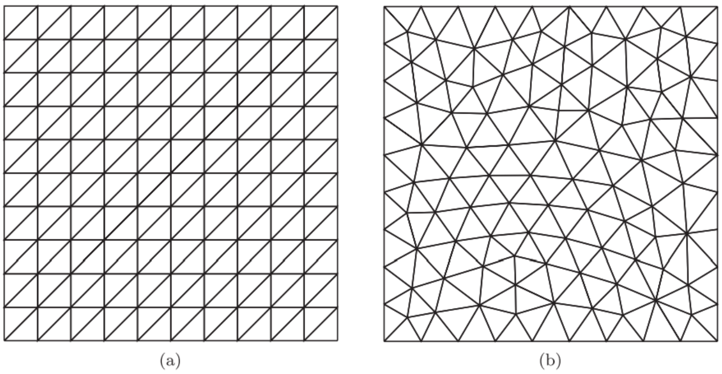

Figure 3.1: Example of a structured (a) and an unstructured (b) mesh [53].

velocity-inlet used to specify the velocity of flow at the inlet of the domain, it is a Dirichlet boundary condition;

outflow used to model the flow exits where velocity and pressure are not known *a priori*, it is a Neumann boundary condition;

wall used to specify the no-slip condition of stationary walls as the surface of the AUVs or the slip condition (specifying all 3 components of shear stress to 0) in the other fluid domain boundaries. It is a Dirichlet boundary condition for the walls and a Neumann condition for the fluid domain boundaries.

3.4.2 Solver

3.4.2.1 Discretization

As mentioned in section 3.3, the continuous governing equations are converted to a set of discrete equations and the continuous variables transformed to discrete variables, in a process called discretization.

The gradient of a variable is used to discretize the convection and diffusion terms in the flow conservation equations and are computed using one of three methods available in ANSYS Fluent [47]:

- Green-Gauss Cell-Based
- Green-Gauss Node-Based
- Least Squares Cell-Based

The node-based gradients were used in this study as they are known to be more stable with triangular and tetrahedral meshes [47].

ANSYS Fluent also allows the user to choose the discretization scheme for the convection terms of each governing equation. The software stores values of a variable at cell centers, as it needs the face values for the convection terms it uses the upwind scheme, which means that the face value is derived from quantities in the cell upstream. There are several upwind schemes available: first-order upwind, second-order upwind, power law and QUICK [47], explained here in detail:

First-order upwind provides a first order precision and the face value is set equal to the center value of the cell upstream;

Second-order upwind provides a second order precision and face value is computed using a multidimensional linear reconstruction approach. Having worse convergence than first-order upwind scheme, it yields more accurate results, especially on triangle and tetrahedral meshes [47];

Power law is based on Péclet number, which is the ratio of the advective to the diffusive transport rates, changing the cell center weights in the interpolation, whose scheme is a power law equation;

QUICK is based on weighted average of second-order upwind and central interpolations of the variable, based on an equation that has a parameter θ. At the limits, for $\theta = 1$ corresponds the central second-order interpolation scheme and for $\theta = 0$ the second-order upwind scheme. QUICK is used for quadrilateral and hexahedral meshes where unique upstream and downstream faces and cells can be identified;

Third order MUSCL uses a parameter θ, similarly to QUICK, to blend a central differencing scheme and second-order upwind scheme, but can be used for arbitrary meshes. It can produce overshoot and undershoot when the flow has discontinuities such as shock waves.

3.4.2.2 Pressure-based solver

ANSYS Fluent allows the user to choose between pressure-based solver and density-based solver. In the pressure-based solver, which is the one used in this study, the pressure field is extracted by solving a pressure (or pressure correction) equation obtained by manipulating the momentum and continuity equations in such a way that the velocity field, corrected by the pressure, satisfies the continuity [47]. This is called the projection method.

The pressure-based solver allows the choice of solving the flow problem in a coupled or segregated way. The pressure-velocity coupling algorithms available in ANSYS Fluent are SIMPLE, SIMPLEC, PISO, Coupled and FSM (Fractional Step method), of which all but Coupled use the pressure-based segregated algorithm [47]., explained here

SIMPLE uses a relationship between velocity and pressure corrections to enforce mass conservation and to obtain the pressure field [47];

SIMPLEC in some problems can converge to a solution faster than SIMPLE through under-relaxation of the pressure-correction. However, it can lead to instability due to high grid skewness;

PISO for transient flows and high degree of distortion meshes in steady-state and transient flows;

Coupled uses pressure-based coupled algorithm instead of segregated one. It obtains a more robust and efficient single-phase implementation for steady-state flows;

FSM for unsteady flows using the non-iterative time advancement scheme [47].

In this study, the SIMPLEC algorithm was used as it provided faster and more accurate results.

3.4.2.3 Turbulence model $k - \epsilon$

Turbulent flows are defined by fluctuating quantities that can be of small scale and high frequency, demanding excessive computational resources to simulate directly. The governing equations can be modified by many techniques such as time-averaging to generate equations less computationally expensive to solve, but carrying additional unknown variables that require turbulence models to be determined.

ANSYS Fluent provides several choices of turbulence models and in this study the standard $k - \epsilon$ with enhanced wall treatment was used. It is considered an industry standard model for general purpose simulations, offering good compromise between numerical effort and accuracy. It is a two equation model, meaning that it uses two additional transport equations to represent the turbulent properties of the flow. The turbulence kinetic energy, k, is the variance of the fluctuations in velocity and the turbulence eddy dissipation, ϵ, is the rate at which this velocity fluctuations dissipate. The values of k and ϵ are calculated by equations (3.5) and (3.6) [44,47],

$$\frac{\partial}{\partial t}(\rho k) + \frac{\partial}{\partial x_i}(\rho k u_i) = \frac{\partial}{\partial x_j}\left[\left(\mu + \frac{\mu_t}{\sigma_k}\right)\frac{\partial k}{\partial x_j}\right] + G_k + G_b - \rho\epsilon - Y_M + S_k \tag{3.5}$$

$$\frac{\partial}{\partial t}(\rho \epsilon) + \frac{\partial}{\partial x_i}(\rho \epsilon u_i) = \frac{\partial}{\partial x_j}\left[\left(\mu + \frac{\mu_t}{\sigma_\epsilon}\right)\frac{\partial \epsilon}{\partial x_j}\right] + C_{1\epsilon}\frac{\epsilon}{k}(G_k + C_{3\epsilon}G_b) - C_{2\epsilon}\rho\frac{\epsilon^2}{k} + S_\epsilon \tag{3.6}$$

where G_k is the generation of turbulence kinetic energy due to the mean velocity gradients, G_b the generation of turbulence kinetic energy due to buoyancy, Y_M the contribution of the fluctuating dilatation in compressible turbulence to the overall dissipation rate, σ_k and σ_ϵ are the turbulent Prandtl numbers for k and ϵ, respectively, S_k and S_ϵ are user-defined source terms and $C_{1\epsilon}$, $C_{2\epsilon}$, and $C_{3\epsilon}$ are constants [47].

Turbulent flows are greatly affected by the presence of walls as in this zone the solution variables have large gradients and the momentum and other scalar transports are stronger, making the accuracy of the near-wall region flow representation of extreme significance [47].

The near-wall region can be divided into three sublayers as represented in Figure 3.2.

There are two traditional approaches to near-wall modeling. In the wall function approach the viscosity-affected region (viscous and buffer sublayers) is not resolved but instead bridged by the wall functions whereas in the near-wall model approach that region is resolved with a mesh that thins all the way to the wall [47]. Figure 3.3 depicts this in a schematic way.

The enhanced wall treatment, available in ANSYS Fluent, used in this study combines these two approaches so it can be used with coarse meshes and fine meshes that resolve the viscosity-affected region all the way to the wall [47].

3.4.2.4 Convergence

In a CFD simulation it is essential to assess convergence to ensure the accuracy of the results while saving computational effort by avoiding simulation past satisfactory accuracy. In ANSYS Fluent, the default convergence criteria requires that the scaled residual,

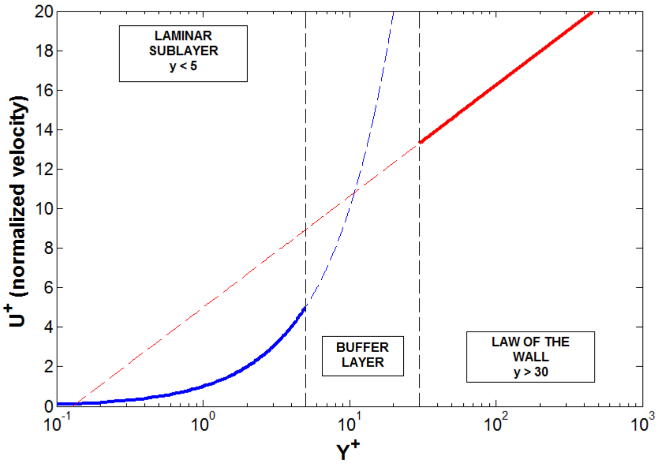

Figure 3.2: Divisions of the near-wall region [47].

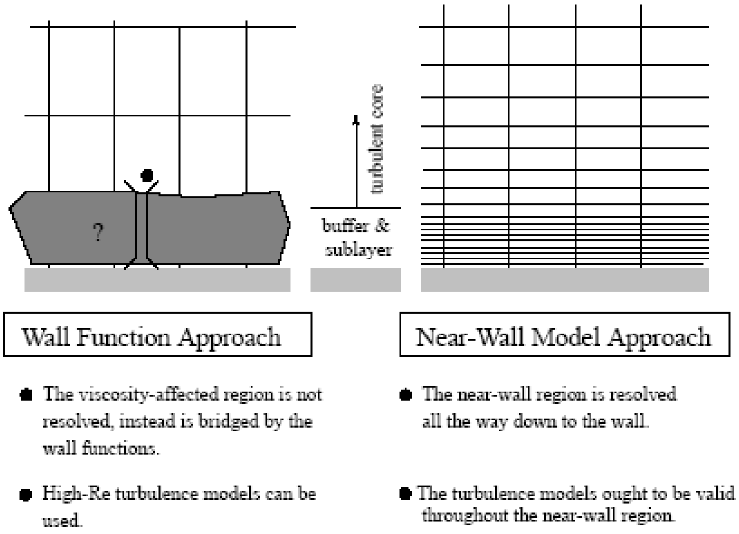

Figure 3.3: Near-wall treatments [47].

R^{ϕ}, defined by equation (3.7) is below 10^{-3} for all equations except energy which must be below 10^{-6} [47].

$$R^{\phi} = \frac{\sum_{\text{cells } P} \left| \sum_{\text{nb}} a_{\text{nb}} \phi_{\text{nb}} + b - a_P \phi_P \right|}{\sum_{\text{cells } P} \left| a_P \phi_P \right|} \tag{3.7}$$

This criterion, however, is not appropriate for all problems and the scaled residual values must be adjusted. A preferred method to assess convergence is to monitor integrated quantities that are relevant to the problem in question such as drag force or a temperature, using the residuals as additional indicators. ANSYS Fluent also allows the user to normalize the residual by dividing it by the maximum residual value for the first N iterations as defined in equation (3.8).

In this study, appropriate quantities were monitored in order to assess convergence.

$$\overline{R^{\phi}} = \frac{R^{\phi}}{max(R^{\phi}_{N=5})} \tag{3.8}$$

3.4.3 Post-processing

The post-processing necessary for this study was performed using ANSYS Fluent, ANSYS CFD Post, Microsoft Excel and MATLAB. The tools available in these software allowed the data extraction and the creation of plots and figures here presented.

Chapter 4

Numerical validation

The main objective of this chapter is to validate the numerical model for flows of water immersed AUVs in ANSYS Fluent. To do so, torpedo shaped AUVs were chosen for the simplicity and extensive literature available.

The numerical work of Madan et al. [54] was selected to serve as reference for the validation as it performed a comparison of drag force, lift force and pitching moment based on results from experimental data and semi-empirical methods developed by Allen and Perkins [55–57], Hopkins [58] and Jorgensen [59] for different AUV hull lengths and angles of attack. More importantly, it also performed CFD analysis for drag and lift force for one AUV geometry and compared it to experimental data and Hopkins method [58].

The geometry of the AUV hulls is composed of three parts: nose, mid-body and tail where the mid-body is of constant diameter and the nose and tail parts are streamlined-shaped. Table 4.1 presents the dimensions of nose, mid-body and tail sections of the AUV for each aspect ratio (total length over maximum diameter, L/D), as provided by Madan [54]. Figure 4.1 shows the geometry and dimensions of an AUV hull of $L/D = 8.5$.

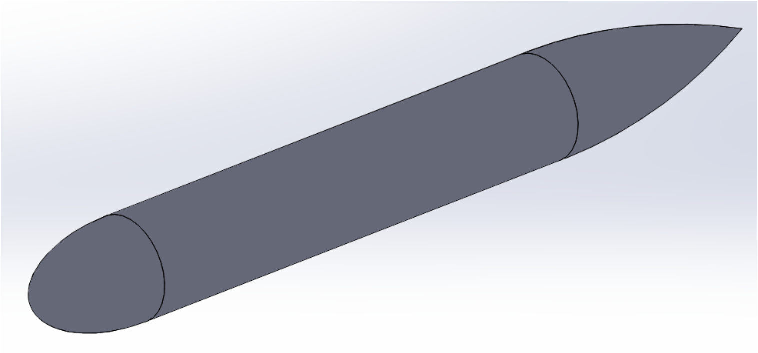

Figure 4.1: Geometry and dimensions of an AUV hull of $L/D = 8.5$.

CFD analysis were performed for a select number of angles of attack (0, 5, 10 and 15 degrees) for one geometry ($L/D = 8.5$) and for 0 degrees of angle of attack for the other geometries ($L/D = 10.5$ and $L/D = 12.5$), in order to approach the CFD, experimental and semi-empirical data available.

As neither equations nor points are provided to model all the AUV parts, an image data extraction tool was used to get (x,y) points from the nose and tail figures of

Table 4.1: Dimensions of nose, mid-body and tail sections for each AUV aspect ratio.

L/D Ratio	Nose length [mm]	Mid-body length [mm]	Tail length [mm]	Total length [mm]
8.5	220	1010	494	1724
10.5	220	1416	494	2130
12.5	220	1822	494	2536

Madan [54] and those were compared to Huang et al. [11] afterbody offsets and Myring equations [12] for both the nose and tail zones. The equations and points were plotted and the comparison is presented in Figures 4.2 for the nose shape.

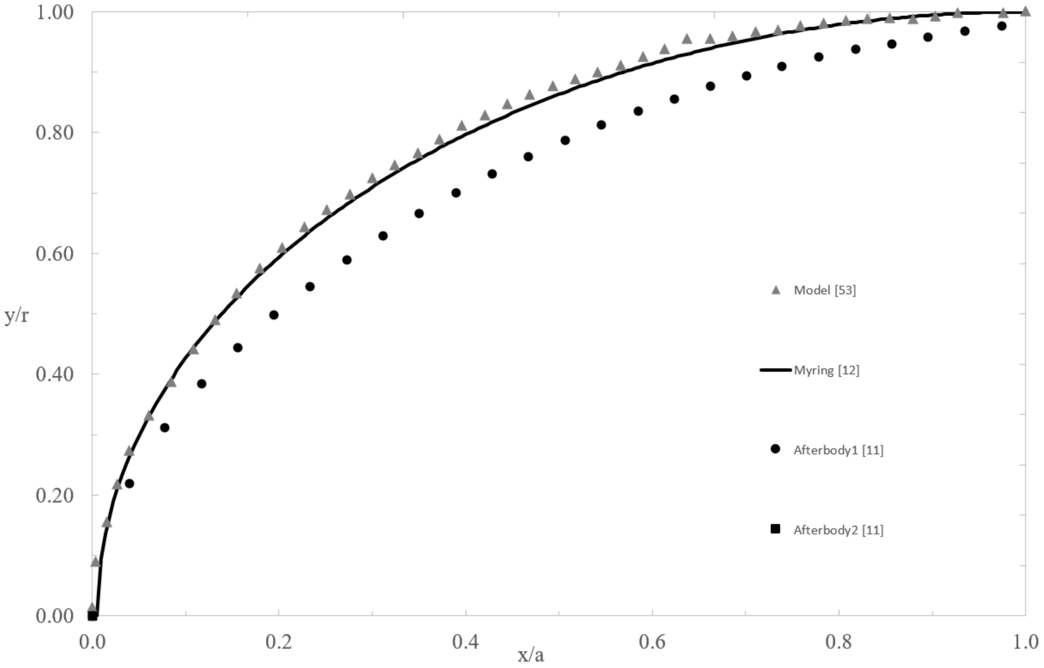

Figure 4.2: Comparison of several nose shapes to the one presented in Madan [54], where r is the radius and a is the total nose length.

For the nose shape, it is easily observed that the Myring equation for the nose (equation 4.1) is a near perfect fit for the nose form, the error possibly being from imperfect data extraction from the figure. The equation is:

$$r = \frac{1}{2} d \left\{ 1 - \left(\frac{x-a}{a} \right)^2 \right\}^{1/n} \tag{4.1}$$

where d is the maximum diameter, x the distance measured along the body axis from nose tip, a the length of nose and n is the index of nose shape, which in this case takes the value of 2.

For the tail shape, neither Myring equation nor Huang afterbody models significantly approach the shape from Madan [54] so a second-order polynomial regression was performed resulting in an excellent approximation ($R^2 = 0.9999$). The polynomial equation is given by

$$y = -0.4333612 \cdot x^2 + 1.0760919 \cdot x - 0.5666583 \tag{4.2}$$

The 3D CAD models of the AUVs were created using SolidWorks and imported into ANSYS Fluent in STEP file format. A tetrahedral mesh of about 512k elements was created with a domain of 40Dx10Dx10D, where D is the diameter, similar to Madan [54], containing a body of influence of 16Dx3Dx3D for the 8.5 model and 18Dx3Dx3D for the 10.5 and 12.5 models, face sizing and inflation layers to correctly capture the boundary layer.

As only an academic license of ANSYS Fluent was available for this work and it has a maximum of 512k elements limitation, a mesh dependence study was performed to evaluate the confidence in the 512k elements mesh and the results are shown in Figure 4.3. It shows a convergence towards high quality meshes and that the error of drag force calculation of the adopted mesh is inferior to 0.5% of the value for a 2.5 million elements mesh, therefore it can be used with confidence in the results.

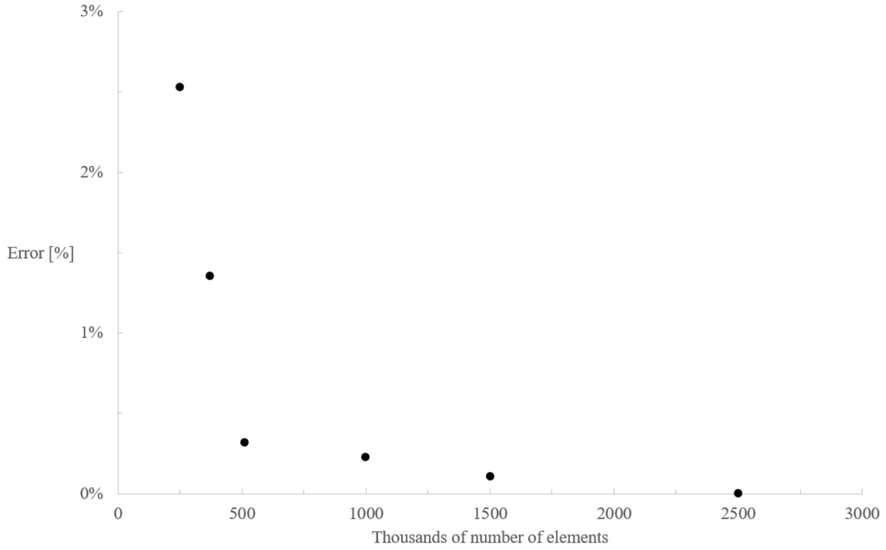

Figure 4.3: Relative error of drag force for each mesh compared to the 2.5 million mesh.

The data from Madan et al. [54] was compared to the results obtained in ANSYS Fluent. The comparison for the 8.5 model is presented in Figures 4.4 and 4.5 and table 4.2, the latter also providing the comparison for the other models.

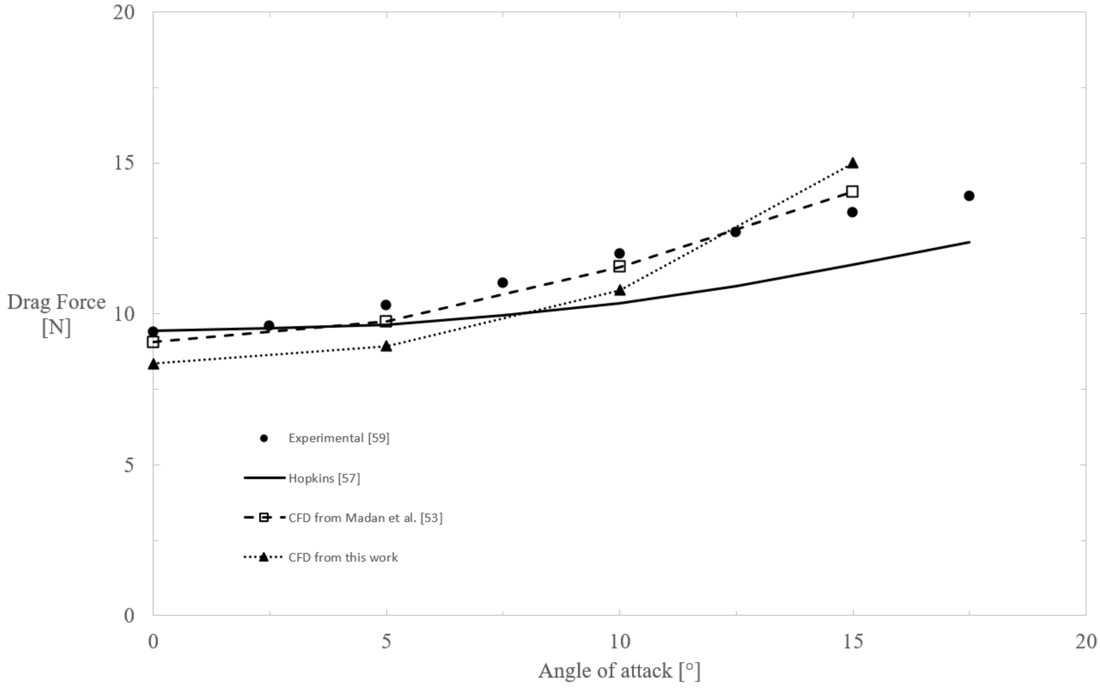

Figure 4.4: Comparison of obtained drag force results and results from Madan et al. [54], for the 8.5 model.

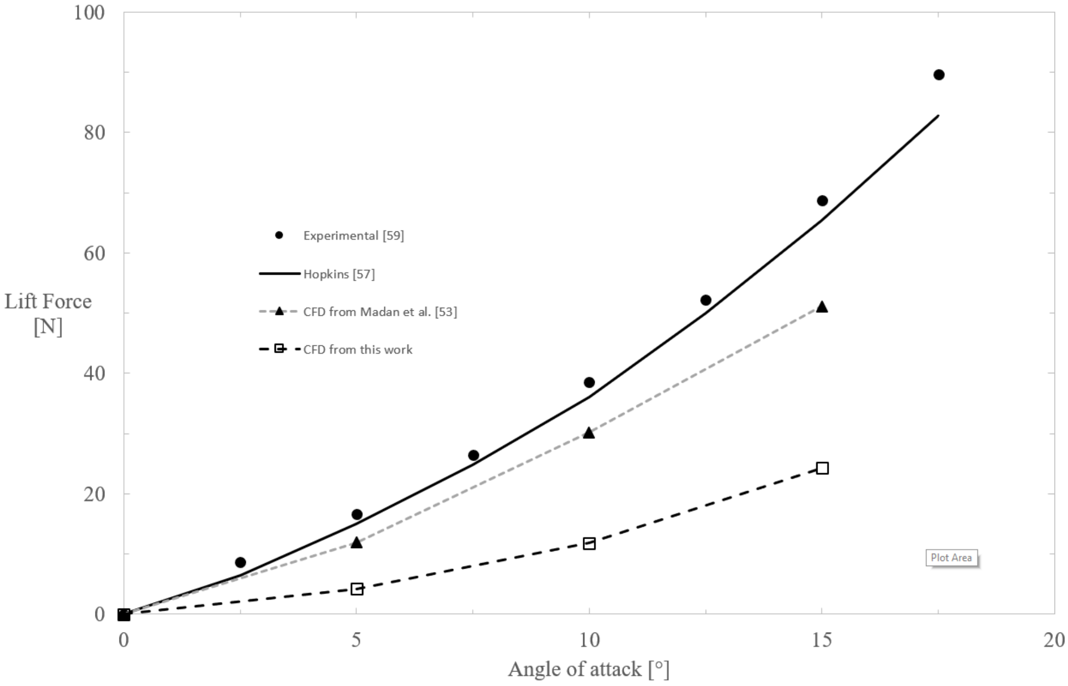

Figure 4.5: Comparison of obtained lift force results and results from Madan et al. [54], for the 8.5 model.

Table 4.2: Comparison of obtained drag force results and results from Madan et al. [54], for all AUV models.

Geometry		CFD	Experimental [60]		Hopkins [58]		CFD Madan et al. [54]	
L/D	Angle	Drag [N]	Drag [N]	Error	Drag [N]	Error	Drag [N]	Error
8.5	0º	8.4	9.4	12%	9.4	13%	9.1	8%
8.5	5º	8.9	10.3	15%	9.6	8%	9.7	9%
8.5	10º	10.8	12.0	11%	10.4	4%	11.5	7%
8.5	15º	15.0	13.4	11%	11.6	22%	14.0	6%
10.5	0º	10.1	10.6	5%	10.1	0%	-	-
12.5	0º	11.6	11.6	0%	11.0	5%	-	-

For the drag force, the results show a reasonably good agreement between all results, with the maximum error relative to the CFD results from Madan et al. [54] being below 10%. For the lift force, however, there is a high disparity between the results obtained and the ones presented in Madan et al. [54], for which no conclusion was identified.

Due to this discrepancy of lift force results, an additional validation was performed using an experimental and CFD study of hydrodynamic coefficients over comparable AUV hulls carried out by Jagadeesh et al. [61]. The hull form considered is the Afterbody1 by Huang et al. [11] already referred above with a length and diameter of 1.4 and 0.14 meters, respectively, giving an aspect ratio of 10. Figure 4.6 shows the used model and Figure 4.7 shows the mesh used.

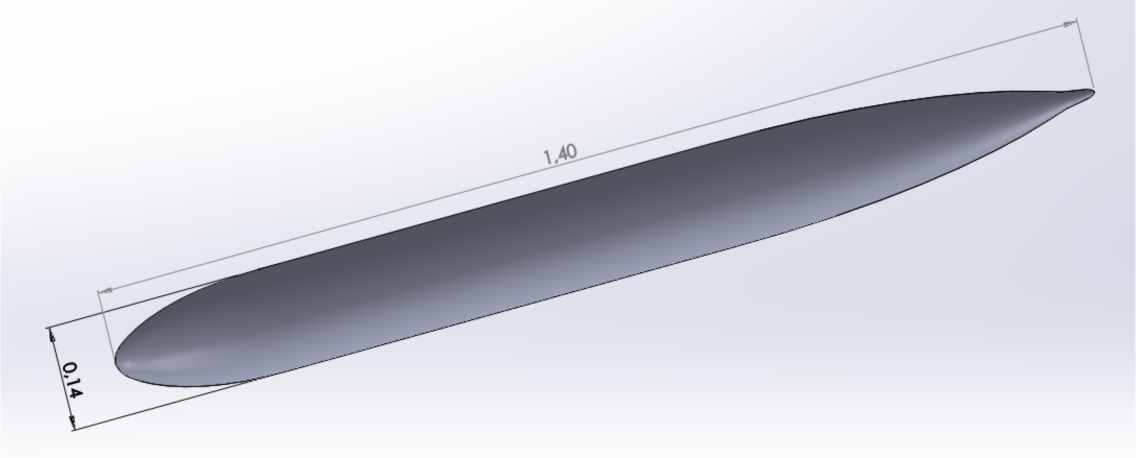

Figure 4.6: Geometry and dimensions of the hull model used in Jagadeesh et al. [61].

Jagadeesh et al. [61] performed experimental and numerical studies for AUV operating speeds ranging from 0.4 m/s to 1.4 m/s ($Re = 1.05 \cdot 10^5$ to $Re = 3.67 \cdot 10^5$) with a 0.2 m/s step for each angle of attack (0°, 5°, 10° and 15°). They collected data for drag, lift and pitching moment coefficient and the reference area, A_{ref} used to calculate the coefficients was

$$A_{ref} = V^2/3 \tag{4.3}$$

where V is the AUV volume.

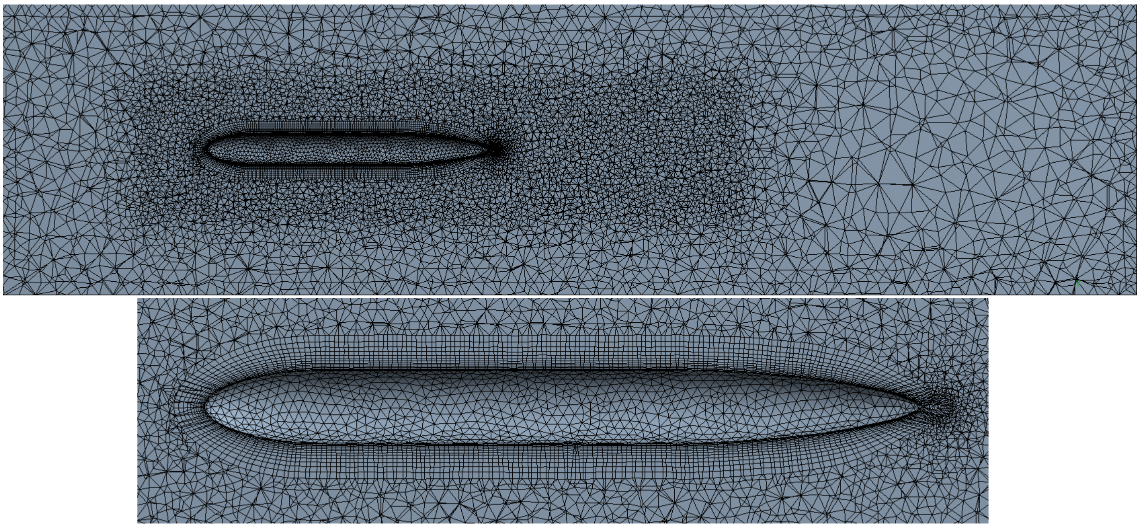

Figure 4.7: Mesh used in ANSYS Fluent.

The same simulations were performed for all velocities and angles of attack and the comparison between the results of this work and the numerical and experimental results from Jagadeesh et al. [61] are present in Table 4.3 for the drag coefficient and in Table 4.4 for the lift coefficient. The error displayed is relative to the CFD results from Jagadeesh et al. [61]. Figures 4.8 and 4.9 present this comparison in the form of plot for drag and lift, respectively.

Table 4.3: Comparison of obtained drag coefficient results and results from Jagadeesh et al. [61] for all velocities and angles of attack.

	0°				5°			
Velocity [m/s]	Exp. [61]	CFD [61]	CFD	Error	Exp. [61]	CFD [61]	CFD	Error
0.4	0.0489	0.0489	0.0505	3%	0.0549	0.0557	0.0539	3%
0.6	0.0451	0.0452	0.0445	1%	0.0513	0.0519	0.0481	7%
0.8	0.0434	0.0441	0.0421	5%	0.0486	0.0500	0.0455	9%
1	0.0419	0.0423	0.0408	3%	0.0471	0.0480	0.0438	9%
1.2	0.0407	0.0412	0.0393	4%	0.0461	0.0469	0.0421	10%
1.4	0.0389	0.0399	0.0381	4%	0.0454	0.0459	0.0408	11%
	10°				15°			
Velocity [m/s]	Exp. [61]	CFD Jag	CFD	Error	Exp. [61]	CFD [61]	CFD	Error
0.4	0.0668	0.0689	0.0634	8%	0.0863	0.0889	0.0851	4%
0.6	0.0634	0.0644	0.0585	9%	0.0829	0.0829	0.0802	3%
0.8	0.0617	0.0622	0.0553	11%	0.0790	0.0799	0.0759	5%
1	0.0594	0.0596	0.0529	11%	0.0774	0.0782	0.0740	5%
1.2	0.0574	0.0581	0.0539	7%	0.0763	0.0767	0.0722	6%
1.4	0.0565	0.0570	0.0494	13%	0.0740	0.0742	0.0705	5%

Table 4.4: Comparison of obtained lift coefficient results and results from Jagadeesh et al. [61] for all velocities and angles of attack.

	0				5			
Velocity [m/s]	Exp.	CFD Jag	CFD	Error	Exp.	CFD Jag	CFD	Error
0.4	-	-	-	-	0.0386	0.0438	0.0218	50%
0.6	-	-	-	-	0.0379	0.0431	0.0212	51%
0.8	-	-	-	-	0.0374	0.0428	0.0207	52%
1	-	-	-	-	0.0369	0.0423	0.0201	53%
1.2	-	-	-	-	0.0364	0.0406	0.0198	51%
1.4	-	-	-	-	0.0354	0.0391	0.0195	50%
	10				15			
Velocity [m/s]	Exp.	CFD Jag	CFD	Error	Exp.	CFD Jag	CFD	Error
0.4	0.0757	0.0787	0.0560	29%	0.1118	0.1173	0.1143	3%
0.6	0.0742	0.0765	0.0573	25%	0.1086	0.1160	0.1145	1%
0.8	0.0727	0.0760	0.0547	28%	0.1061	0.1153	0.1091	5%
1	0.0718	0.0750	0.0540	28%	0.1047	0.1151	0.1112	3%
1.2	0.0705	0.0747	0.0509	32%	0.1029	0.1146	0.1133	1%
1.4	0.0695	0.0747	0.0536	28%	0.1002	0.1141	0.1137	0%

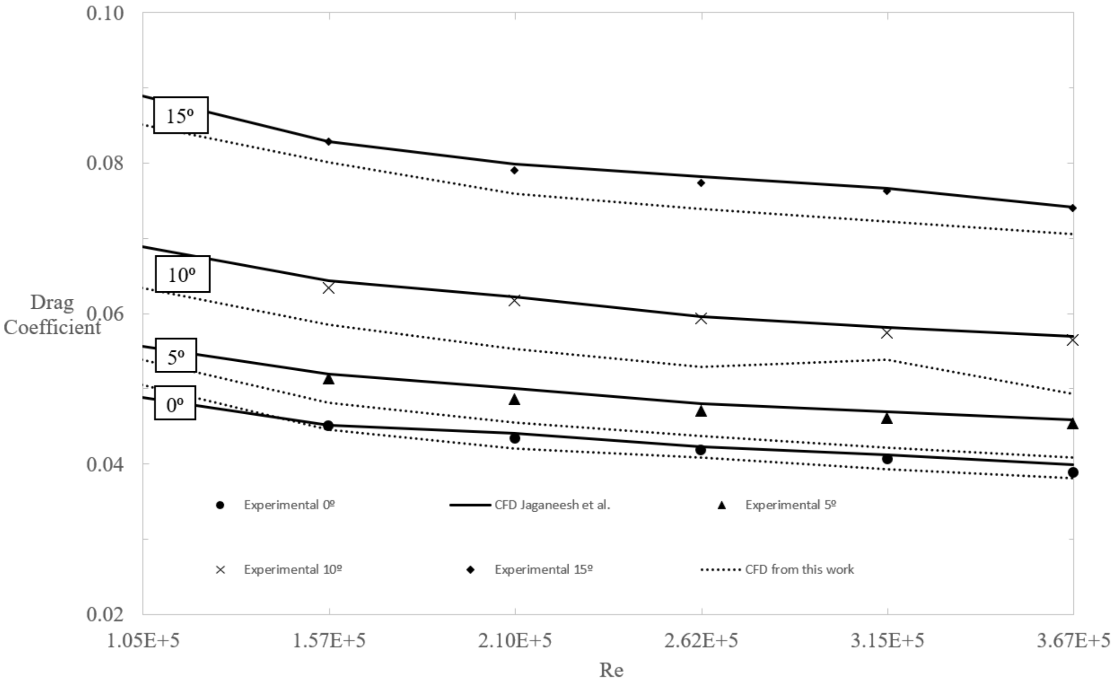

Figure 4.8: Plot of obtained drag coefficient results and both experimental and numerical results from [61] for all velocities and angles of attack.

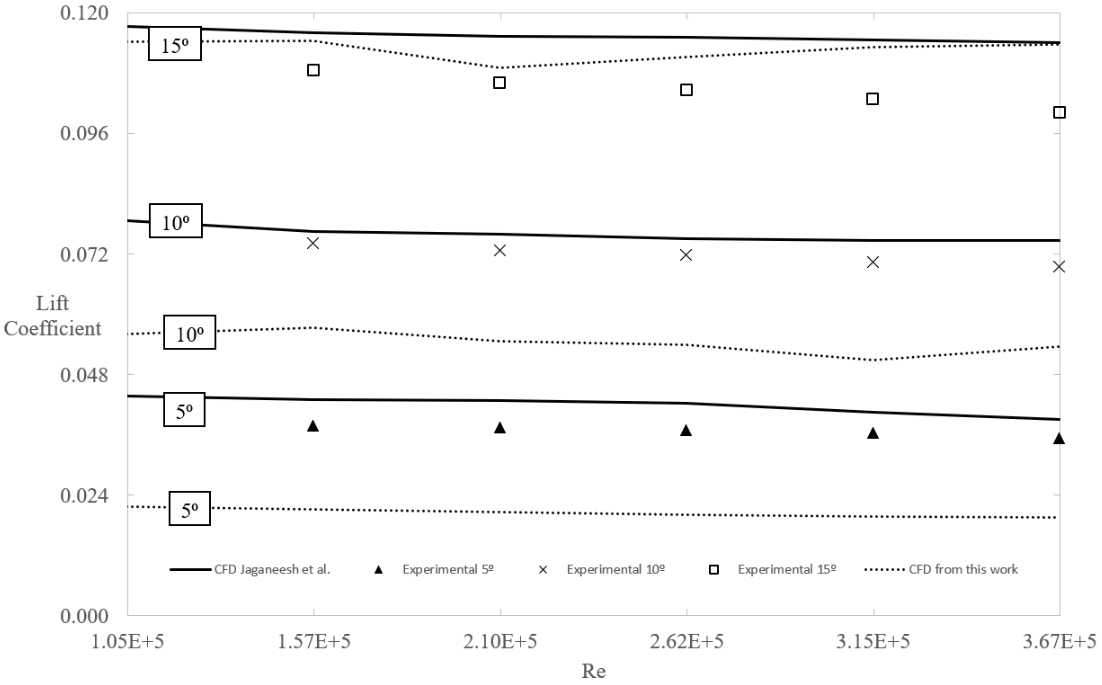

Figure 4.9: Plot of obtained lift coefficient results and both experimental and numerical results from [61] for all velocities and angles of attack except 0°.

The drag coefficient results show a good approximation to the results from Jagadeesh et al. [61] as most of them have error below 10%. The lift coefficient, as before, shows the same disparity of results, however, only for low angles of attack. The higher the angle, and thus higher the lift coefficient, the lower the disparities are.

In conclusion, the drag results are satisfactory for both studies, having an average error of all simulations of 6%, with the maximum at 13%. The lift results, however, are unacceptable with errors up to 50% in some cases. Nevertheless, this does not present great influence on the next study as only axial direction force is analyzed.

Chapter 5

Anguilliform swimming performance

Anguilliform swimmers propel themselves forward by generating a transverse wave towards the posterior part of the body while the anterior part remains straight [62]. They can even swim backwards by reversing the direction of the wave [63]. These marine species are known for their maneuverability and dexterous movement and so they present a great swimming mode to inspire AUVs, particularly in confined spaces such as aquaculture environments and seafloor wreckage.

This chapter presents the results of a numerical study on *anguilliform* motion, for different sets of Reynolds and Strouhal numbers, i.e. different tail-beat frequencies and swimming velocities.

5.1 Simulation setup

Based on the literature review of section 2.2.2, the adopted motion for this work was equation (2.5),

$$h(x,t) = a\left[\sin\left(2\pi\left(\frac{1}{\lambda/L}\frac{x}{L} - ft\right)\right) - \sin\left(2\pi\left(\frac{x}{L} - ft\right)\right)\right] \tag{2.5}$$

based on the work of Vorus and Taravella [20], with the parameters $a = 0.1$ and $\lambda/L = 0.8$. Figure 5.1 shows the body centerlines at different moments of the cycle t/T, where $T = 1/f$ is the cycle period.

The geometry of a cylindrical body of 1 meter of length and 60 millimeters of diameter was created with a shape given by equation (2.5) at time $t = 0$

$$h(x,0) = 0.1\left[\sin\left(\frac{2\pi}{0.8}x\right) - \sin\left(2\pi x\right)\right] \tag{5.1}$$

and imported into ANSYS Design Modeler as an *.step* file, where the flow domain geometry was created. Figure 5.2 displays the geometry and Figure 5.3 shows the mesh used.

A mostly tetrahedral mesh was generated using proper body and face sizings and inflation layer. In the solver, ANSYS Fluent, the dynamic mesh capability was used to simulate the effect of the body oscillation in the fluid using smoothing and remeshing methods. The mesh motion is controlled by an User-Defined Function (UDF) which uses equation (2.5) to define the movement of the eel. This UDF was modified from the

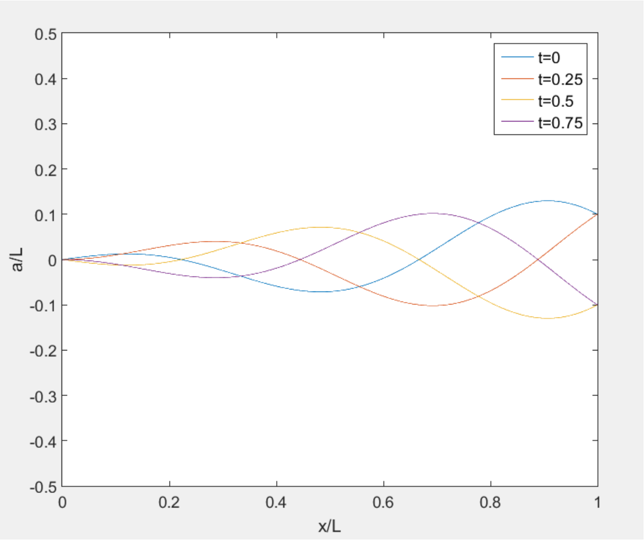

Figure 5.1: Body centerlines at times $t/T = 0, 0.25, 0.5, 0.75$.

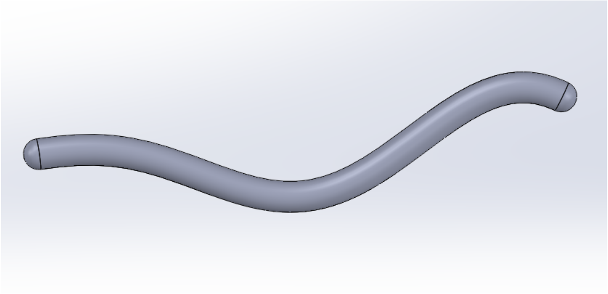

Figure 5.2: Geometry at time $t = 0$.

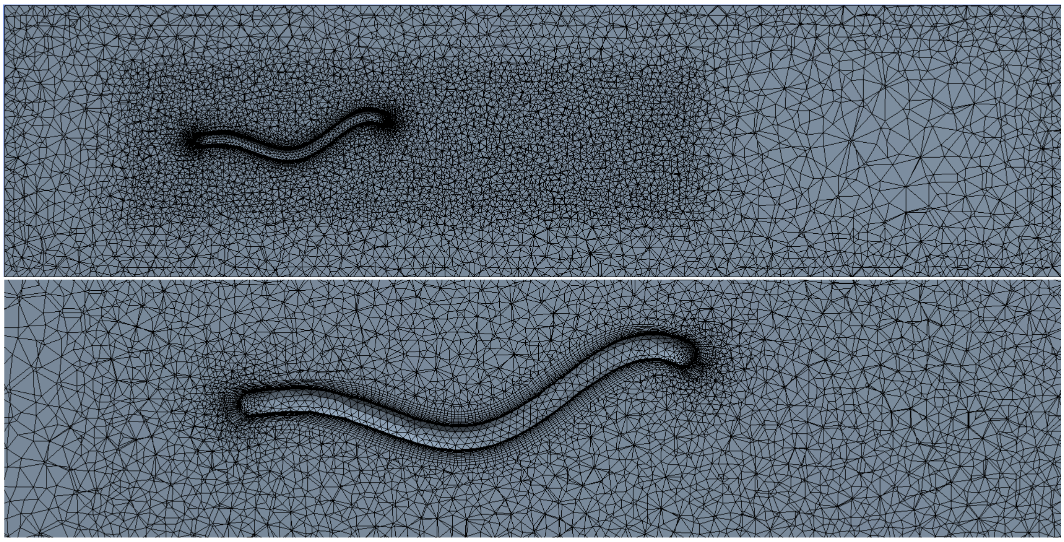

Figure 5.3: Mesh used in ANSYS Fluent.

one used in Rogers [64] to parameterize the flow/swimming velocity, nondimensionalized by the Reynolds number and the frequency, nondimensionalized by the Strouhal number. The code is available in Appendix A.

In order to decompose the force into thrust and drag and study its efficiency, the necessary variables were defined in ANSYS Fluent using the Custom Field Functions and Report Definitions.

Simulations were performed for $Re = 500, 2000, 4000, 8000$. $Re = 4000$ is also used in the analysis from Borazjani and Sotiropoulos [24], so a comparison can be made. For each Reynolds number, a large interval of Strouhal numbers were studied, making sure to capture the critical Strouhal number, St_{crit}. These include the $St = 0$ case which corresponds to the case where the body is rigid and is virtually pulled through the water at velocity U. Various swimming cycles were simulated until the force coefficient, $C_F = F(t)/\rho U^2 L^2$, differences between two consecutive cycles were acceptable. In the results presented, the average of the absolute force coefficient temporal differences between two consecutive cycles are below 5%. Figure 5.4 shows the last three cycles of a simulation, as an example.

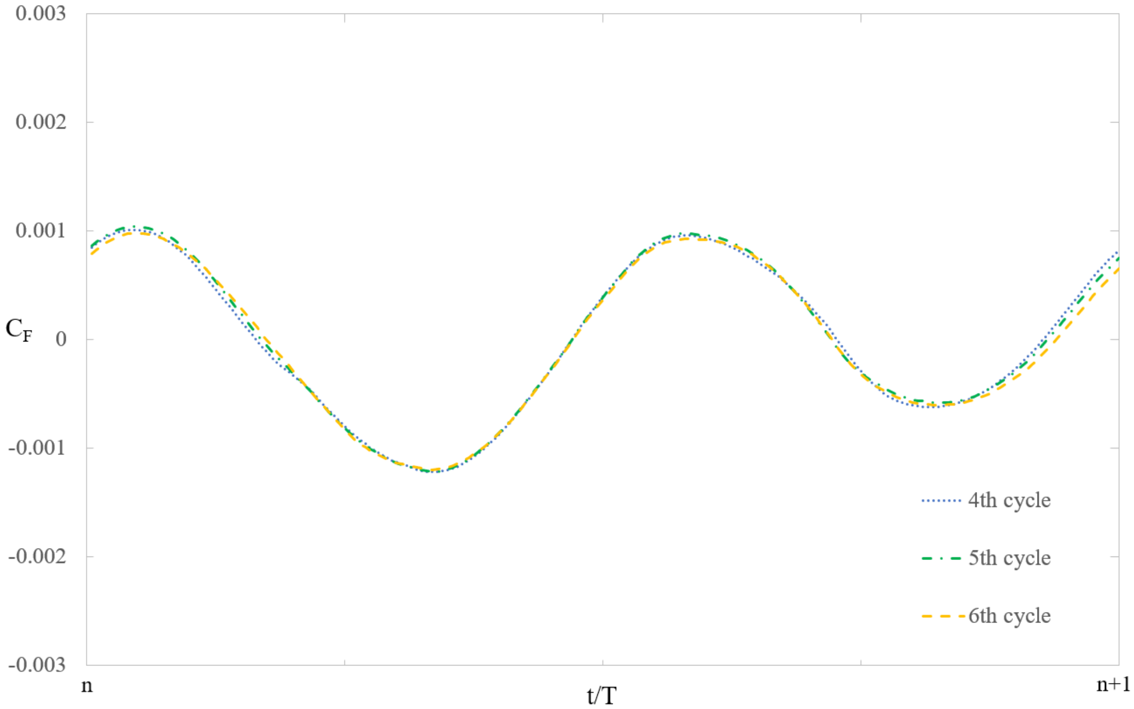

Figure 5.4: Time evolution of the force coefficient for the last three cycles of a simulation where the average of temporal differences between all three is below 5%.

Figures 5.5 through 5.8 show the time evolution of the instantaneous force coefficient, C_F, normalized by the C_F of the rigid body, $C_F^{St=0}$, for the four different Re values. This relative force coefficient allows for a better analysis of the results. A value below -1 means that the body has a higher drag than the rigid body due to the undulations and vice-versa, while a value above or below 0 means the force on the body is thrust dominant or drag dominant, respectively.

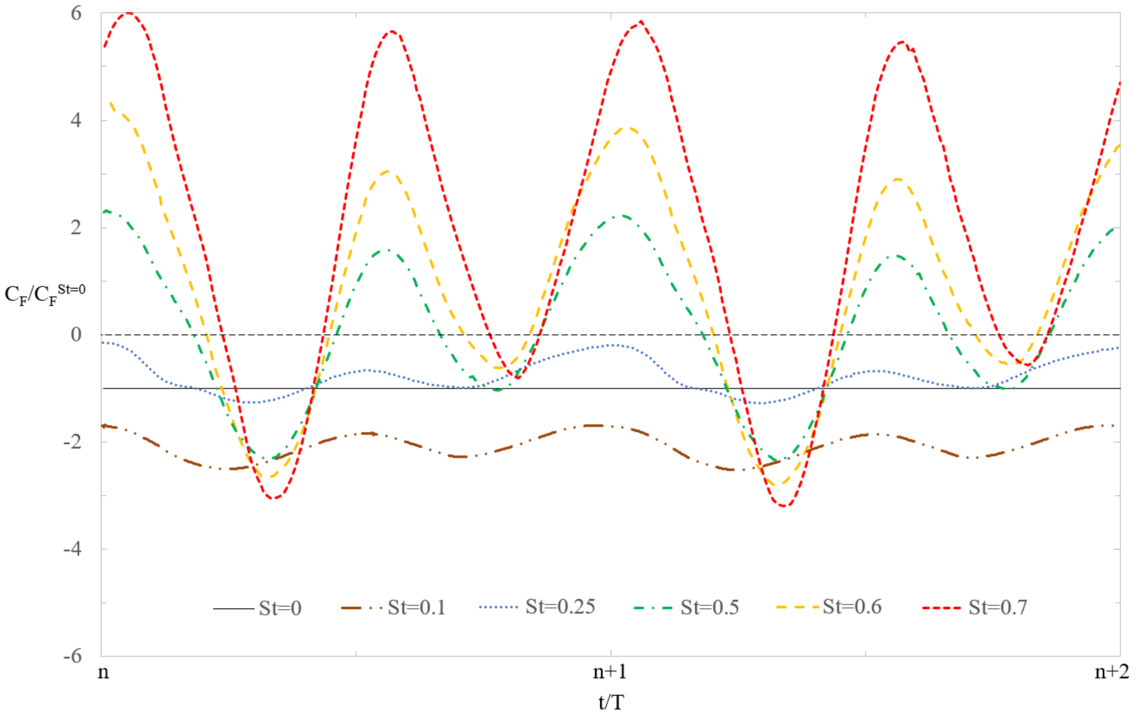

Figure 5.5: Time evolution of normalized force coefficients of different *St* values, for $Re = 500$.

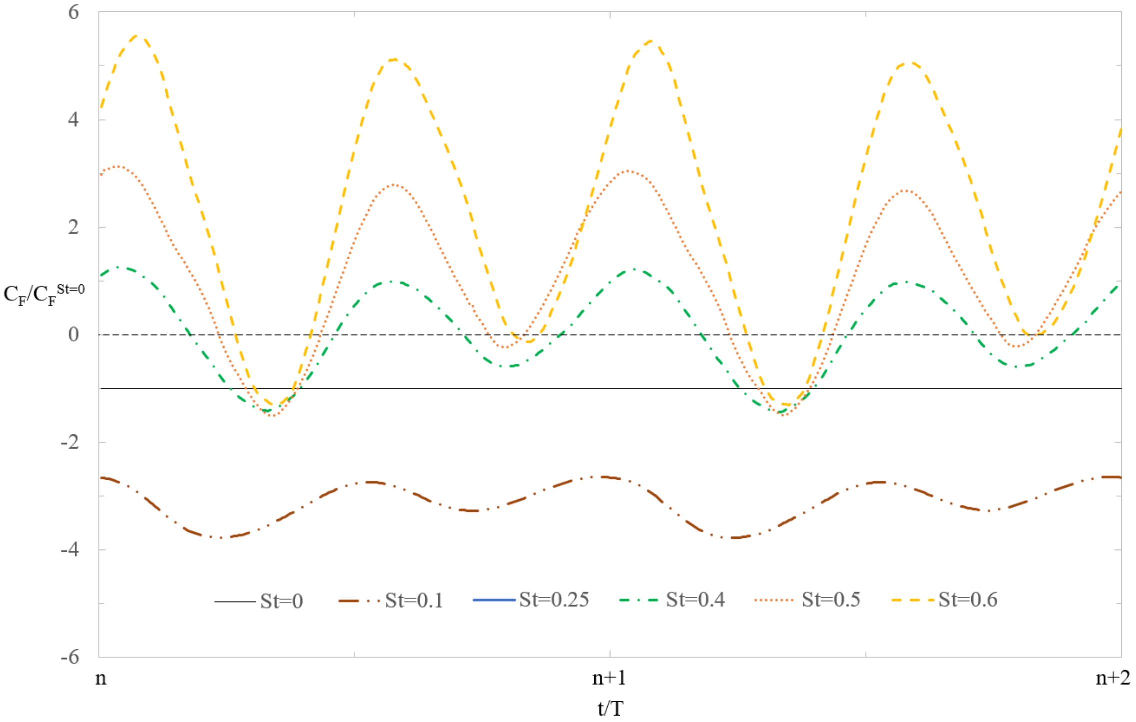

Figure 5.6: Time evolution of normalized force coefficients of different *St* values, for $Re = 2000$.

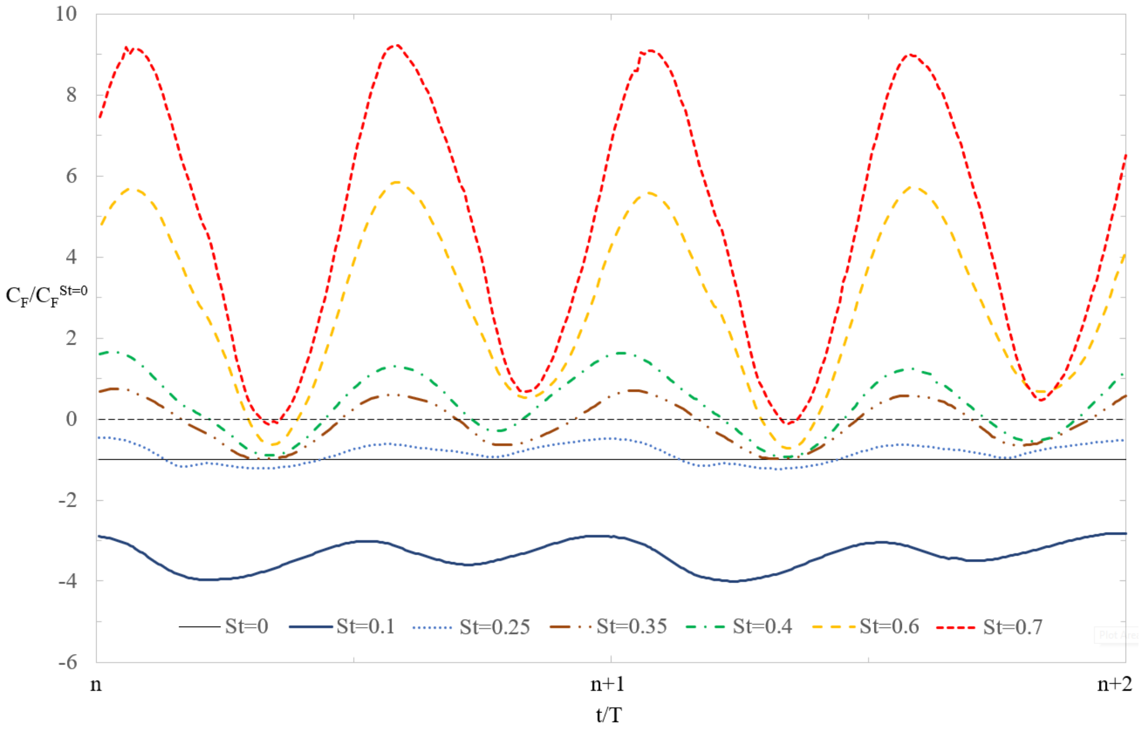

Figure 5.7: Time evolution of normalized force coefficients of different *St* values, for *Re* = 4000.

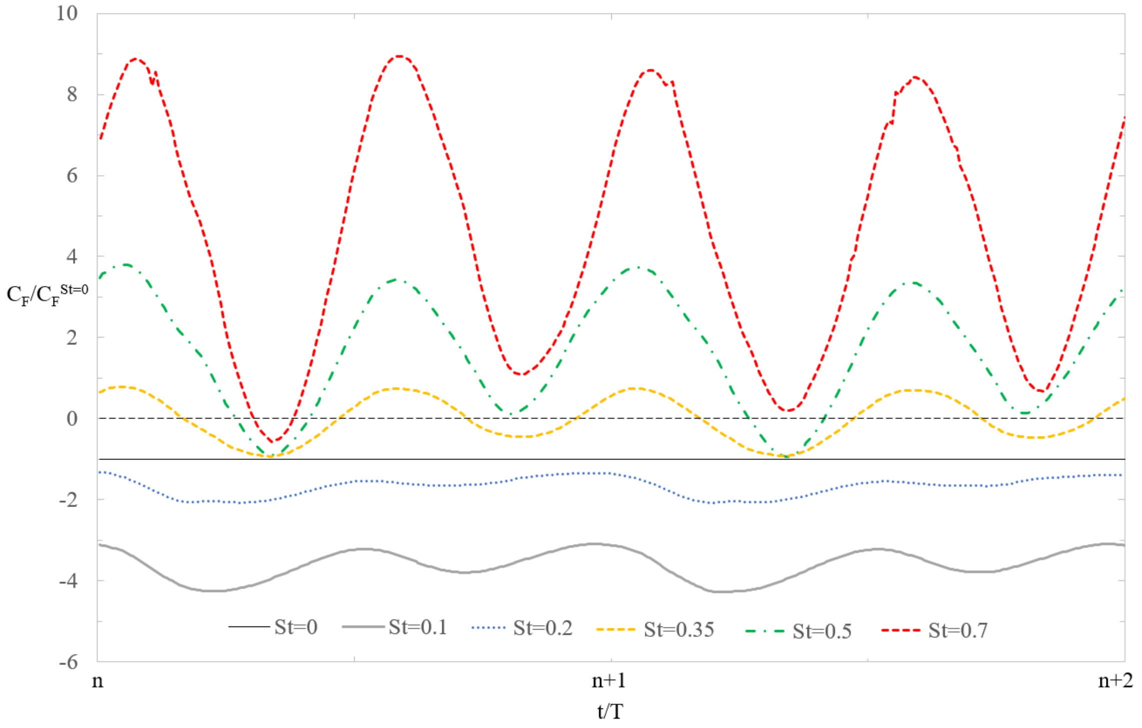

Figure 5.8: Time evolution of normalized force coefficients of different *St* values, for *Re* = 8000.

For all *Re* values, at low *St* values the tail-beat frequency is so low that the drag component of the force overcomes any thrust force produced and the resultant force is of drag-type and greater in absolute value than that of the rigid body case, as documented by Borazjani and Sotiropoulos [24]. Further increase of Strouhal number causes increasingly higher force coefficient mean values and amplitudes. Eventually the resultant force is positive meaning more thrust is produced than drag. The value of *St* at which this transition occurs is the critical Strouhal number, as introduced above.

Figure 5.9 shows how the time averaged normalized force coefficient evolves with increasing *St* and allows for an approximate determination of the critical Strouhal number. The time averaged values are from the latest cycle.

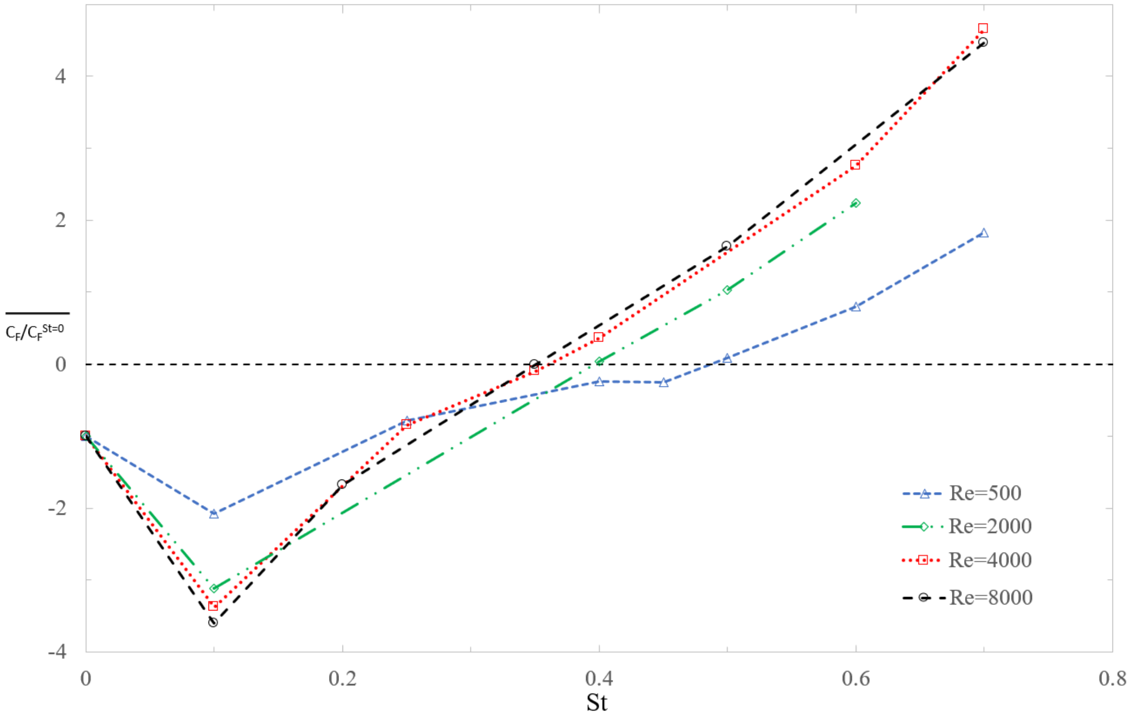

Figure 5.9: Time averaged normalized force coefficient evolution by *St*, for all *Re*.

It can be seen that the St_{crit} value is a decreasing function of the Reynolds number, as stated by Borazjani and Sotiropoulos [24]. This is even more clear in Figure 5.10 where it can also be seen that St_{crit} tends asymptotically to a value close to 0.35.

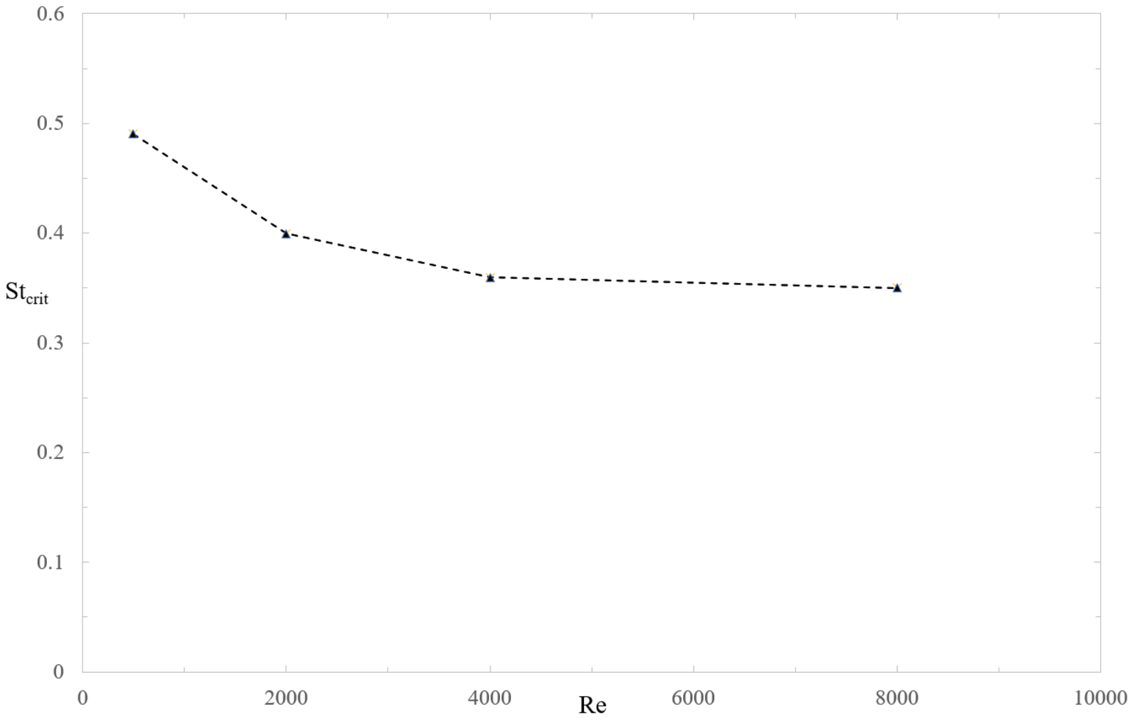

Figure 5.10: Evolution of the critical Strouhal number, St_{crit}, with the number of Reynolds, Re.

The critical Strouhal number is approximately 0.49, 0.40, 0.36 and 0.35 for $Re = 500, 2000, 4000, 8000$, respectively, which is close to the typical Strouhal number values of *anguilliform* swimmers, documented in literature (0.3-0.5) [65,66].

The St_{crit} value for $Re = 4000$, approximately 0.49, is lower than the one from Borazjani and Sotiropoulos, 0.62 [24], however, this is most likely due to the dissimilarities in the geometry, parameters and motion equation. Nevertheless, in that work, the critical Strouhal number values only approach the literature values at $Re = \infty$, which corresponds to inviscid flow, while here the St_{crit} values approach at real flow with typical swimming velocities.

Figures 5.11 and 5.12 show the velocity contours at the end of a cycle for $St = 0.1$ and $St = 0.4$, respectively, for $Re = 4000$.

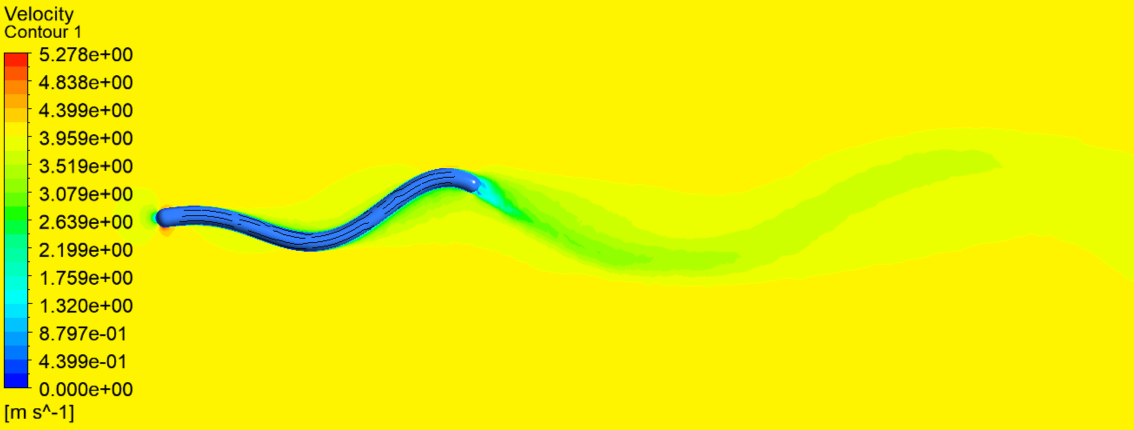

Figure 5.11: Velocity contour for $St = 0.1$ at $Re = 4000$.

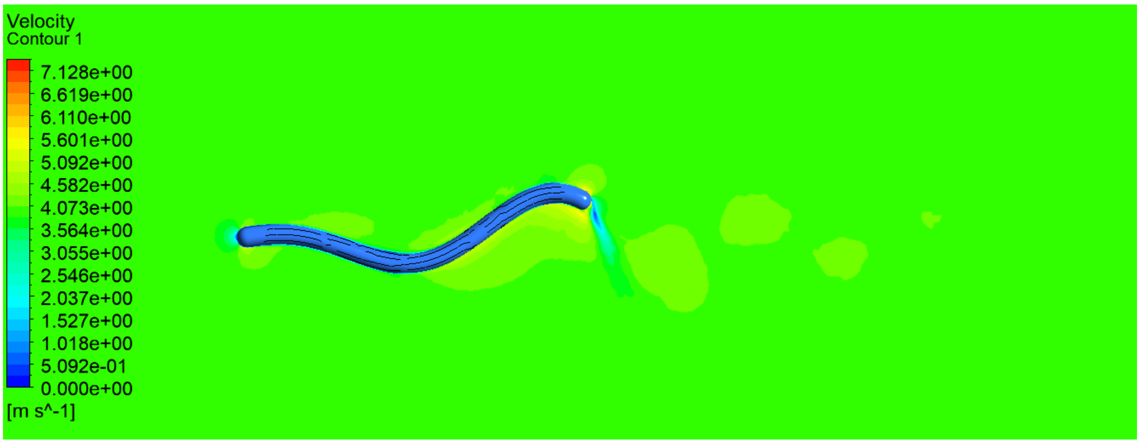

Figure 5.12: Velocity contour for $St = 0.4$ at $Re = 4000$.

It is visible that for low frequencies, the wake is smooth while for higher frequencies vortex shedding starts to appear.

The Froude efficiency given by equation 2.13 was calculated for $Re = 2000, 4000, 8000$ and compared with some efficiency results from Borazjani and Sotiropoulos [24] as well as the calculated efficiency values using elongated body theory equations (2.14 and 2.15). The results are displayed in table 5.1.

Table 5.1: Comparison between calculated Froude efficiency from this work and from Borazjani and Sotiropoulos [24], as well as, from EBT theory equations.

Re	η_{CFD}	$\eta_{Borazjani}$	η_{EBT}	η_{EBT-2}
300	-	17.62%	70.00%	69.95%
2000	61.62%	-	75.00%	74.93%
4000	38.39%	31.62%	78.57%	78.49%
8000	36.25%	-	78.57%	78.49%

It can be seen that for the only comparable value, $Re = 4000$, the efficiency result is quite close to the result from Borazjani and Sotiropoulos [24]. Despite this work not having a result for a lower Re than 2000, the results from Borazjani and Sotiropoulos [24] allow the conclusion that the efficiency has a maximum around $Re = 2000$. The results from EBT theory equations show a high disparity with the calculated results and do not capture the peak at around $Re = 2000$ as they are inviscid methods.

Chapter 6

Conclusion and future work

6.1 Conclusion

The first objective of this study was to get insight on the performance of traditional AUVs as well as on numerical modeling. A validation of a numerical model was then necessary for later simulations. Two different studies were performed, each one with several angle of attack and velocity conditions. In both, the drag force/coefficient results were satisfactory, having a good similarity with the literature documented values [54, 61], an average error between all simulations of 6%. The lift force/coefficient results contained a large error, up to 50% in some cases, particularly at low angles of attack, while at higher angles (15°) the results showed good agreement. The cause of this error was extensively studied but no conclusion was identified.

The second and main objective of this study was to perform an analysis on the swimming performance of *anguilliform* swimming with different conditions, namely tail-beat frequency and swimming velocity. Different swimming motion and parameters were found in the literature, having selected the motion described by Vorus and Taravella [20] while comparing the results to the ones from Borazjani and Sotiropoulos [24].

The results showed a good agreement, the discrepancies possibly being due to different motion, parameters and geometry. The simulations for low Strouhal number showed small amplitudes on the force coefficient, meaning the body can swim smoother at low tail-beat frequencies and, as expected, at this lower frequencies the force is of drag-type, meaning the body does not produce sufficient thrust to propel itself. In fact, at low enough St values, the drag is so dominant over thrust that the body has higher drag than a rigid body being towed at the same velocity. As Strouhal number is increased, the thrust component of the force becomes ever more present until it overcomes the drag component. The St at which this occurs, the critical Strouhal number, St_{crit}, is approximately 0.49, 0.40, 0.36 and 0.35 for $Re = 500, 2000, 4000, 8000$, respectively, being very close to the values of which live *anguilliform* swimmers usually swim at, based on literature. The St_{crit} is a decreasing asymptotic function of Re that tends to a value close to 0.35. The Froude efficiency peaks around $Re = 2000$, which is in the transitional flow regime.

This information provides a good understanding of the conditions at which a bio-inspired AUV based on *anguilliform* swimming motion can swim and be efficient, being valuable in the concept of the vehicle.

6.2 Future work

In the future, the availability of a commercial license could potentially provide greater quality and reliability to the results obtained, as a more refined mesh could be employed. More simulations should be performed at different Reynolds numbers as well as different Strouhal numbers to have a superior understanding of the swimming performance at different conditions that will be demanded of the bio-inspired vehicle. It will also allowed for a better characterization of the critical Strouhal number evolution with the Reynolds number, which will be of considerable importance to the definition of the operating points.

Finally, other swimming motions must be studied, particularly the *thunniform* swimming motion for the reasons already stated, using the same analysis, making possible a comparison between the two modes on performance and efficiency. This comparison will be useful for defining when is worth to change modes during an operation.

Appendices

Appendix A

Mesh motion UDF

```c
#include "udf.h"
#include "math.h"

/* Modified from original code of Charles Rogers, University of New Orleans.
*/

double displacement (double x , double t ) {

  double L, a, U, St, pi, xbar, tbar, A, B, velocity, strouhal, lambdaL, f;

  St = RP_Get_Input_Parameter("strouhal");
 U = RP_Get_Input_Parameter("velocity");

  L=1;          //length of the body
  lambdaL=0.8;      //lambda/L : wavenlength / length
  a=0.1;          //tail amplitude / length

  f=St*U/(2*a);     //tail beat frequency

  pi = 3.141592654;

  xbar = x/L;       //nondimensional x
  tbar = f*t;       //nondimensional t

 A = sin(2*pi*((xbar/lambdaL)-tbar));
  B = sin(2*pi*(xbar-tbar));

  return (a*(A-B));
}


DEFINE_GRID_MOTION(eel_theory, domain, dt, time, dtime)
{

  /* Udf to describe the general motion of the eel in 3D Fluent.
  This is the theoretical motion defined by Vorus at all points, therefore this
     DOES NOT maintain the shape over time.
  */

  Thread *tf = DT_THREAD(dt);
  face_t f;
```

```
Node *node_p;

double xprev, yprev, hprev, d, h;
int n;

  /* Variables:
    xprev = previous time step x position of the node
    yprev = previous time step y position of the node
    hprev = previous time centerline displacement at a given x
    d = distance between the centerline and the node
    h = current time centerline displacement
  */

SET_DEFORMING_THREAD_FLAG (THREAD_T0(tf));

begin_f_loop(f, tf)
{
  f_node_loop (f, tf, n)
  {
    node_p = F_NODE(f, tf, n);
    if (NODE_POS_NEED_UPDATE (node_p))
    {
      NODE_POS_UPDATED(node_p);
      if (CURRENT_TIME > 0)
      {
        if (NODE_X ( node_p ) <= 0.0)
        {
          // No change, these nodes stay in
          // the same spot
          continue;
        }
        else if (NODE_X ( node_p ) > 1.0)
        {
          // Previous time position
          xprev = NODE_X(node_p);
          yprev = NODE_Y(node_p);

          // Calculate the previous time
          // centerline displacement at x = 1.0
          hprev = displacement(1.0,PREVIOUS_TIME);

          // Calculate the difference between the
          // node and the centerline
          d = yprev - hprev;

          //Calculate the new time
          //centerline displacement
          h = displacement(1.0,CURRENT_TIME);

          // Use the distance calculation to
          // give the new node y postition
          NODE_Y (node_p) = h + d;
        }
        else
        {
          // Get the x and y position of the
          // node to be moved
          xprev = NODE_X (node_p);
```

```
            yprev = NODE_Y (node_p);

            // Calculate the previous time
            // centerline displacement
            hprev = displacement(xprev, PREVIOUS_TIME);

            // Caluclate the difference between
            // the node and the centerline
            d = yprev - hprev;

            // Calculate the new time
            // centerline displacement
            h = displacement(xprev, CURRENT_TIME);

            // Use the distance calculation
            // to give the new node y position
            NODE_Y (node_p) = h + d;
          }
        }
      }
    }
  }
  end_f_loop (f, tf);
}
```

Bibliography

[1] Yuxiang Deng. A bio-inspired swimming robot concept design for marine aquaculture applications, 2014. Available at `https://ntnuopen.ntnu.no/ntnu-xmlui/handle/11250/274116`.

[2] G. Li, Y. Deng, O. L. Osen, S. Bi, and H. Zhang. A bio-inspired swimming robot for marine aquaculture applications: From concept-design to simulation. In *OCEANS 2016 - Shanghai*, pages 1–7, April 2016.

[3] Levi DeVries, Michael Kutzer, Rebecca E. Richmond, and Archie C. Bass. Design, modeling, and experimental drag characterization of a bio-inspired, shape-adapting underwater vehicle. ASME 2018 International Design Engineering Technical Conferences and Computers and Information in Engineering Conference. Volume 5A: 42nd Mechanisms and Robotics Conference. Quebec City, Quebec, Canada. 08 2018.

[4] Baofeng Liao, Zheng Li, and Ruxu Du. Robot fish with a novel biomimetic wire-driven flapping propulsor. *Advanced Robotics*, 28, 01 2013.

[5] National University of Singapore. Nus-developed manta ray robot swims faster and operates up to 10 hours. Available at `http://news.nus.edu.sg/press-releases/NUS-robotic-manta-ray`, accessed: 2019-02-27.

[6] Jessiko by robotswim. Available at `http://www.robotswim.com`, accessed: 2019-02-27.

[7] Snorri Gudmundsson. Chapter 15 - aircraft drag analysis. In Snorri Gudmundsson, editor, *General Aviation Aircraft Design*, pages 661 – 760. Butterworth-Heinemann, Boston, 2014.

[8] Volker Bertram. Submarine hull design, Norwegian University of Science and Technology. Available at `https://www.ntnu.edu/documents/20587845/1266707380/2012Chennai_SubmarineDesign.pdf/9bb180be-a08d-48ea-af4e-7e5e19210d3b`, accessed: 2019-05-15.

[9] P.N. Joubert. Some Aspects of Submarine Design Part 2: Shape of a submarine 2026. Defence Science and Technology Organisation, Australian Government: Department of Defense. 05 2019.

[10] Australian Maritime College. Fluid mechanics submarine design, 2011. Available at `https://samueldavey.files.wordpress.com/2013/04/fluid-dynamics-submarine-report.pdf`, accessed: 2019-05-19.

[11] T.T. Huang, N. Santelli, and G. Belt. Stern boundary-layer flow on axisymmetric bodies. *National Academy of Sciences*, Proceedings of the Twelfth ONR Symposium on Naval Hydro-dynamics, 1978.

[12] D. F. Myring. A theoretical study of body drag in subcritical axisymmetric flow. *The Aeronautical Quarterly*, Volume 27, Issue 3:pp. 186–94, 14, 15, 43., 08 1976.

[13] Michael Sfakiotakis, David M. Lane, and John Davies. Review of fish swimming modes for aquatic locomotion. *Oceanic Engineering, IEEE Journal of*, 24:237 – 252, 05 1999.

[14] C. M. Breder. *The locomotion of fishes*. Zoologica, 4, 4th edition, 1926.

[15] William Hoar and David Randall. *Fish Physiology*, volume 7th, Locomotion. Zoologica, 4, 1979.

[16] Richard Clapman and Huosheng Hu. Biomimetic Design for Efficient Robotic Performance in Dynamic Aquatic Environments - Survey. Technical Report: CES-529. School of Computer Science, Electronic Engineering, University of Essex. 2013.

[17] Guoyuan Li, Yuxiang Deng, Ottar Osen, Shusheng Bi, and Houxiang Zhang. A bio-inspired swimming robot for marine aquaculture applications: from concept-design to simulation. Proceedings of the OCEANS 2016-Shanghai. Shanghai, China. IEEE 2016, pp. 1-7. 04 2016.

[18] J. E. Colgate and K. M. Lynch. Mechanics and control of swimming: a review. *IEEE Journal of Oceanic Engineering*, 29(3):660–673, July 2004.

[19] Sujoy Saha and G.P. Celata. Advances in modelling of biomimetic fluid flow at different scales. *Nanoscale research letters*, 6:344, 04 2011.

[20] William S. Vorus and Brandon M. Taravella. Anguilliform fish propulsion of highest hydrodynamic efficiency. *Journal of Marine Science and Application*, 10:163–174, 06 2011.

[21] Marcus Hultmark, Megan Leftwich, and Alexander Smits. Flowfield measurements in the wake of a robotic lamprey. *Experiments in fluids*, 43:683–690, 11 2007.

[22] Eric Tytell and George Lauder. The hydrodynamics of eel swimming. i. wake structure. *The Journal of experimental biology*, 207:1825–41, 06 2004.

[23] C S. Wardle, John Videler, and J D. Altringham. Tuning in to fish swimming waves: body form, swimming mode and muscle function. *The Journal of experimental biology*, 198:1629–36, 02 1995.

[24] Iman Borazjani and Fotis Sotiropoulos. Numerical investigation of the hydrodynamics of anguilliform swimming in the transitional and inertial flow regimes. *Journal of Experimental Biology*, 212(4):576–592, 2009.

[25] Iman Borazjani and Fotis Sotiropoulos. Numerical investigation of the hydrodynamics of carangiform swimming in the transitional and inertial flow regimes. *Journal of Experimental Biology*, 211(10):1541–1558, 2008.

[26] M J Lighthill. Hydromechanics of aquatic animal propulsion. *Annual Review of Fluid Mechanics*, 1:413–446, 11 2003.

[27] JY Cheng and Reinhard Blickhan. Note on the calculation of propeller efficiency using elongated body theory. *The Journal of experimental biology*, 192:169–77, 08 1994.

[28] Virginia Institute of Marine Science. What is an AUV? Available at `https://www.vims.edu/research/units/legacy/cornwallis/auv/index.php`, acessed: 2019-06-02.

[29] Russell B. Wynn, Veerle A.I. Huvenne, Timothy P. Le Bas, Bramley J. Murton, Douglas P. Connelly, Brian J. Bett, Henry A. Ruhl, Kirsty J. Morris, Jeffrey Peakall, Daniel R. Parsons, Esther J. Sumner, Stephen E. Darby, Robert M. Dorrell, and James E. Hunt. Autonomous underwater vehicles (auvs): Their past, present and future contributions to the advancement of marine geoscience. *Marine Geology*, 352:451 – 468, 2014. 50th Anniversary Special Issue.

[30] J. Bellingham. *Autonomous Underwater Vehicles (AUVs)*. Encyclopedia of Ocean Sciences, pp. 212-216. 12 2001.

[31] Stephen Wood. *Autonomous Underwater Gliders*. in Underwater Vehicles, pp. 499-524. 01 2009. In-Tech.

[32] International Submarine Engineering. Theseus AUV. Available at `https://ise.bc.ca/product/theseus-auv/`, acessed: 2019-06-02.

[33] INC. HYDROID. REMUS 6000 for Commercial Applications. Available at `https://www.hydroid.com/remus-6000-commercial-applications`, acessed: 2019-06-02.

[34] KONGSBERG. SEAGLIDER C2. Available at `https://www.kongsberg.com/globalassets/maritime/km-products/documents/c2_km_seaglider_datasheet-03052017.pdf`, acessed: 2019-06-02.

[35] ECA Group. A27-M / AUV / Autonomous Underwater Vehicle. Available at `https://www.ecagroup.com/en/solutions/a27-m-auv-autonomous-underwater-vehicle`, acessed: 2019-06-02.

[36] Michael Triantafyllou and George Triantafyllou. An efficient swimming machine. *Scientific American - SCI AMER*, 272:64–70, 03 1995.

[37] J. Kumph and M. S. Triantafyllou. A Fast-Starting and Maneuvering Vehicle, the ROBOPIKE. page 485–490, 1998. Proc. Int. Symp. Seawater Drag Reduct, Newport, RI.

[38] K. H. Low, G Seet, and Chunlin Zhou. Biomimetic design and workspace study of compact and modular undulating fin body segments. 2007 International Conference on Mechatronics and Automation, pp. 129 - 134.

[39] K. Suzumori, S. Endo, T. Kanda, N. Kato, and H. Suzuki. A bending pneumatic rubber actuator realizing soft-bodied manta swimming robot. In *Proceedings 2007 IEEE International Conference on Robotics and Automation*, pages 4975–4980, April 2007.

[40] S.M. Blinder. Chapter 8 - differential equations. In S.M. Blinder, editor, *Guide to Essential Math (Second Edition)*, pages 125 – 149. Elsevier, Oxford, second edition edition, 2013.

[41] Cornell University. Fluent learning modules, 2018. Available at `https://confluence.cornell.edu/display/SIMULATION/FLUENT+Learning+Modules`, accessed: 2019-04-16.

[42] Suzanne Fielding. Durham University. The basic equations of fluid dynamics, 2018. Available at `https://community.dur.ac.uk/suzanne.fielding/teaching/BLT/`, accessed: 2019-04-16.

[43] Inc. ANSYS. ANSYS Fluent 12.0/12.1 User's Guide. Available at `http://www.afs.enea.it/project/neptunius/docs/fluent/html/ug/main_pre.htm`, accessed: 2019-04-18.

[44] Inc. ANSYS. ANSYS 16.2.3 CFX Documentation. Available at `https://www.sharcnet.ca/Software/Ansys/16.2.3/en-us/help/ai_sinfo/cfx_intro.html`, accessed: 2019-05-03.

[45] CFD Direct. Computacional Fluid Dynamics. Available at `https://cfd.direct/openfoam/computational-fluid-dynamics/`, accessed: 2019-04-18.

[46] B.R. Hodges. Hydrodynamical modeling. In *Reference Module in Earth Systems and Environmental Sciences*. Elsevier, 2014.

[47] Inc. Fluent. FLUENT 6.3 User's Guide. Available at `https://www.sharcnet.ca/Software/Fluent6/html/ug/main_pre.htm`, accessed: 2019-05-03.

[48] Anand Shukla, Akhilesh Kumar Singh, and P Singh. A comparative study of finite volume method and finite difference method for convection-diffusion problem. *American Journal of Computational and Applied Mathematics*, 1:67–73, 12 2012.

[49] Jiri Blazek. Chapter 3 - principles of solution of the governing equations. In Jiri Blazek, editor, *Computational Fluid Dynamics: Principles and Applications*, pages 29 – 72. Butterworth-Heinemann, Oxford, third edition, 2015.

[50] Paul G. Tucker. *Pre- and Post-Processing*, page 459–532. Cambridge Aerospace Series. Cambridge University Press, 2016.

[51] Jiyuan Tu, Guan-Heng Yeoh, and Chaoqun Liu. *Computational Fluid Dynamics*. Butter Worth Heinemann, 2nd edition, 2013.

[52] Jiyuan Tu, Guan-Heng Yeoh, and Chaoqun Liu. Chapter 4 - cfd mesh generation: A practical guideline. In Jiyuan Tu, Guan-Heng Yeoh, and Chaoqun Liu, editors, *Computational Fluid Dynamics (Third Edition)*, pages 125 – 154. Butterworth-Heinemann, third edition edition, 2018.

[53] H.R. Hiester, Matthew Piggott, P.E. Farrell, and P Allison. Assessment of spurious mixing in adaptive mesh simulations of the two-dimensional lock-exchange. *Ocean Modelling*, 73:30–44, 01 2014.

[54] Madan A. D and Manoj Issac. Hydrodynamic analysis of auv hulls using semi-empirical and cfd approach. *Universal Journal of Mechanical Engineering*, 5:137–143, 11 2017.

[55] H. Allen and E. Perkins. A study of effects of viscosity on flow over slender inclined bodies of revolution. *National Advisory Committee on Aeronautics (NACA)*, Report No. 1048, 01 1951.

[56] H. Allen and E. Perkins. Characteristics of flow over inclined bodies of revolution. *National Advisory Committee on Aeronautics (NACA)*, Research Memorandum RM A50L07, 03 1951.

[57] H. Allen and E. Perkins. Estimation of the forces and moments acting on inclined bodies of revolution of high fineness ratio. *National Advisory Committee on Aeronautics (NACA)*, Research Memorandum RM A9126, 11 1949.

[58] E. Hopkins. A semi-empirical method for calculating the pitching moment of bodies of revolution at low mach numbers. *National Advisory Committee on Aeronautics (NACA)*, Research Memorandum RM A51C14, 1951.

[59] L. H. Jorgensen. Prediction of static aerodynamic characteristics for space-shuttle-like and other bodies at angles of attack from 00-1800. *National Aeronautics and Space Administration (NASA)*, NASA Technical note (NASA TN D-6996), 1973.

[60] Christopher Williams, T.L. Curtis, Michael Doucet, Manoj Issac, and Farhood Azarsina. Effects of hull length on the hydrodynamic loads on a slender underwater vehicle during manoeuvres. IEEE Ocean Conference, Boston, MA, 2006.

[61] P. Jagadeesh, K. Murali, and V.G. Idichandy. Experimental investigation of hydrodynamic force coefficients over auv hull form. *Ocean Engineering*, 36(1):113 – 118, 2009. Autonomous Underwater Vehicles.

[62] Stefan Kern and Petros Koumoutsakos. Simulations of optimized anguilliform swimming. *The Journal of experimental biology*, 209:4841–57, 01 2007.

[63] J. H. Long Jr, W. Shepherd, and R. G. Root. Manueuverability and reversible propulsion: How eel-like fish swim forward and backward using travelling body waves. 1997. Proc. Special Session on Bio-Engineering Research Related to Autonomous Underwater Vehicles, 10th Int. Symp., 118–134.

[64] Charles Rogers. Computational fluid dynamics analysis of an ideal anguilliform swimming motion, 2014. University of New Orleans Theses and Dissertations.

[65] Frank Fish and George Lauder. Passive and active flow control by swimming fishes and mammals. *Annu. Rev. Fluid Mech*, 38:193–224, 01 2006.

[66] Ulrike K. Müller, Jos G. M. van den Boogaart, and Johan L. van Leeuwen. Flow patterns of larval fish: undulatory swimming in the intermediate flow regime. *Journal of Experimental Biology*, 211(2):196–205, 2008.

Acknowledgements

I would like to express my gratitude to Prof. Dr. Alexandre Afonso for all of the assistance, support and encouragement provided throughout the course of this dissertation, as well as the valuable knowledge shared about Computational Fluid Dynamics.

To Dr. Adriano Lima for all the assistance and for sharing his expertise of both CFD and ANSYS Fluent.

To Eng. Tiago Morais for welcoming me at INEGI and providing me excellent conditions to work on this dissertation.

To my family and friends, for all the support and encouragement throughout, not only this semester, but the whole course.